

RD-A178 288

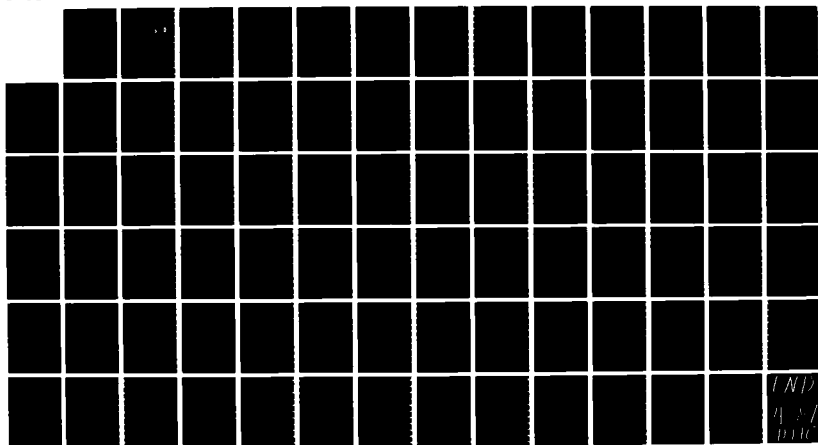
CONSTRAINTS ON MODELING OF UNDERGROUND EXPLOSIONS IN
GRANITE(U) S-CUBED LA JOLLA CA J L STEVENS ET AL.
OCT 86 555-R-87-8312 AFGL-TR-86-0264 F19628-86-C-0038

1/1

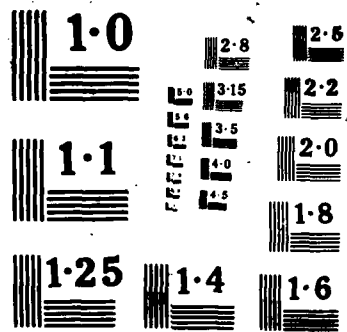
F/8 8/7

ML

UNCLASSIFIED



IND
n
DHC



AD-A178 288

AFGL-TR-86-0264

SSS-R-87-8312

15

CONSTRAINTS ON MODELING OF UNDERGROUND EXPLOSIONS IN GRANITE

J. L. Stevens
N. Rimer
S. M. Day

DTIC
SELECTED
MAR 26 1987
S D
D

S-CUBED
A Division of Maxwell Laboratories, Inc.
P.O. Box 1620
La Jolla, California 92038-1620

October 1986

Semiannual Report No. 1

Approved for Public Release;
Distribution Unlimited.

AIR FORCE GEOPHYSICS LABORATORY
Air Force Systems Command
United States Air Force
Hanscom Air Force Base
Massachusetts 01731

UNCLASSIFIED

AD-A178288

SECURITY CLASSIFICATION OF THIS PAGE

REPORT DOCUMENTATION PAGE

1a REPORT SECURITY CLASSIFICATION Unclassified		1b RESTRICTIVE MARKINGS	
2a SECURITY CLASSIFICATION AUTHORITY		3b DISTRIBUTION AVAILABILITY OF REPORT Approved for Public Release; Distribution Unlimited.	
2b DECLASSIFICATION/DOWNGRADING SCHEDULE			
4 PERFORMING ORGANIZATION REPORT NUMBER(S) SSS-R-87-8312		5 MONITORING ORGANIZATION REPORT NUMBER(S) AFGL-TR-86-0264	
6a NAME OF PERFORMING ORGANIZATION S-CUBED Division of Maxwell Labs., Inc.	6b OFFICE SYMBOL (If applicable)	7a NAME OF MONITORING ORGANIZATION Air Force Geophysics Laboratory/LWH	
7c ADDRESS (City, State, and ZIP Code) P. O. Box 1620 La Jolla, California 92038-1620		7b ADDRESS (City, State and ZIP Code) Hanscom Air Force Base Massachusetts 01731	
8a NAME OF FUNDING/SPONSORING ORGANIZATION Defense Advanced Research Projects Agency	8b OFFICE SYMBOL (If applicable) DSO/GSD	9 PROCUREMENT INSTRUMENT IDENTIFICATION NUMBER F19628-86-C-0038	
10 SOURCE OF FUNDING NUMBERS PROGRAM ELEMENT NO 62714E		PROJECT NO 6A10	TASK NO DA
11 WORK UNIT ACCESSION NO BA			

11 TITLE (Include Security Classification)

CONSTRAINTS ON MODELING OF UNDERGROUND EXPLOSIONS IN GRANITE (U)

12 PERSONAL AUTHOR(S)

J. L. Stevens, N. Rimer and S. M. Day

13a TYPE OF REPORT Semiannual Report #1	13b TIME COVERED FROM 3/10/86 TO 09/10/86	14 DATE OF REPORT (Year, Month, Day) October 1986	15 PAGE COUNT 82
--	--	--	---------------------

16 SUPPLEMENTARY NOTATION

17 COSATI CODES FIELD GROUP SUB-GROUP	18 SUBJECT TERMS (Continue on reverse if necessary and identify by block number) Rock mechanics, Numerical simulation, Granite, Explosion seismology Underground nuclear explosion Dilatancy
--	--

19 ABSTRACT (Continue on reverse if necessary and identify by block number)

This report summarizes our current understanding of the constraints on modeling of underground explosions in granite. Numerical simulations of explosions in granite are compared with near field waveforms from PILEDRIVER, HARDHAT, and SHOAL, and with peak velocity and peak displacement data from the Hoggar explosions. Numerical simulations agree well with the data at close range. At larger ranges the calculations reproduce the shape of the observed waveforms, but overestimate the observed amplitudes.

Dilatancy introduced through the use of an associated flow rule in numerical calculations can make a significant difference in the predicted size of the explosion cavity. The effect is potentially large enough to explain the difference in cavity sizes between the Hoggar explosions and United States granite explosions, however dilatancy also leads to very large near field ground motion, and eliminates overshoot in the explosion source function.

(Continued)

20 DISTRIBUTION/AVAILABILITY OF ABSTRACT <input type="checkbox"/> UNCLASSIFIED/UNLIMITED <input checked="" type="checkbox"/> SAME AS RPT <input type="checkbox"/> DTIC USERS	21 ABSTRACT SECURITY CLASSIFICATION Unclassified	
22a NAME OF RESPONSIBLE INDIVIDUAL James Lewkowicz	22b TELEPHONE (Include Area Code)	22c OFFICE SYMBOL LWH

DD FORM 1473, 84 MAR

83 APR edition may be used until exhausted
All other editions are obsolete

SECURITY CLASSIFICATION OF THIS PAGE

UNCLASSIFIED

SECURITY CLASSIFICATION OF THIS PAGE

18. SUBJECT TERMS (Continued)

Hoggar
Piledriver
Hardhat
Shoal

19. ABSTRACT (Continued)

Dynamic and quasistatic laboratory experiments on explosions in granite are now in progress at SRI International and New England Research Corporation. The current status of these experiments is summarized.

TABLE OF CONTENTS

Section	Page
1. INTRODUCTION AND SUMMARY.....	1
2. CONSTRAINTS ON MODELING OF UNDERGROUND EXPLOSIONS IN GRANITE.....	3
3. THE EFFECT OF DILATANCY ON GROUND MOTION CALCULATIONS IN GRANITE.....	21
4. STATUS OF LABORATORY EXPERIMENTS.....	32
5. REFERENCES.....	35
APPENDIX A: SOME ANALYTIC RESULTS RELEVANT TO SHOCK WEAKENING IN GRANITE.....	37
APPENDIX B: STRAIN PATHS, TIME HISTORIES AND REDUCED DISPLACEMENT POTENTIALS FOR GRANITE CALCULATIONS.....	55

Accession For	
NTIS	CRA&I <input checked="" type="checkbox"/>
DTIC	TAB <input type="checkbox"/>
Unannounced	<input type="checkbox"/>
Justification.....	
By.....	
Distribution/.....	
Availability Codes.....	
Dist	Available or Special
A-1	



LIST OF ILLUSTRATIONS

Figure	Page
1. Near field velocity waveforms from PILEDRIVER compared to waveforms from calculation number 570.....	5
2. Observed near field displacement from PILEDRIVER compared to displacement from calculation number 570.....	6
3. Near field velocity waveforms from HARDHAT compared to waveforms from calculation number 570 scaled to 5.9 kilotons.....	9
4. Near field displacement from HARDHAT compared to displacement from calculation number 570 scaled to 5.9 kilotons.....	10
5. Near field velocity data and displacement data from HARDHAT compared to velocity and displacement from calculation number 570 scaled to 5.9 kilotons.....	11
6. Near field velocity data and displacement data from SHOAL compared to velocity and displacement from calculation number 570 scaled to 12.5 kilotons.....	12
7. Peak velocity data from the Hoggar explosions and from the three United States Granite explosions all scaled to one kiloton plotted as a function of scaled range	13
8. Peak displacement data from the Hoggar explosions and from the three United States Granite explosions all scaled to one kiloton plotted as a function of scaled range	14
9. Failure surface used in calculations estimated from laboratory measurements of Climax Stock granite	16

LIST OF ILLUSTRATIONS (Continued)

Figure	Page
10. Near field velocity data from PILEDRIVER compared with data from a calculation using the laboratory strength of granite with no weakening.....	17
11. Near field displacement data from PILEDRIVER compared with data from a calculation using the laboratory strength of granite with no weakening.....	18
12. Near field velocity data from PILEDRIVER compared with data from a calculation using a strength of 200 bars throughout the calculation	19
13. Near field displacement data from PILEDRIVER compared with data from a calculation using a strength of 200 bars throughout the calculation.....	20
14. Near field velocity data from PILEDRIVER compared with data from a calculation using the laboratory strength of granite and an associated flow rule.....	25
15. Near field displacement data from PILEDRIVER compared with data from a calculation using the laboratory strength of granite and an associated flow rule.....	26
16. Near field velocity data from PILEDRIVER compared with data from a calculation using a failure surface with a slope of 0.5 and a radial return flow rule.....	28
17. Near field displacement data from PILEDRIVER compared with data from a calculation using a failure surface with a slope of 0.5 and a radial return flow rule.....	29

LIST OF ILLUSTRATIONS (Concluded)

Figure	Page
18. Near field velocity data from PILEDRIVER compared with data from a calculation using a failure surface with a slope of 0.5 and an associated flow rule.....	30
19. Near field displacement data from PILEDRIVER compared with data from a calculation using a failure surface with a slope of 0.5 and an associated flow rule.....	31

LIST OF TABLES

Table	Page
1. United States Explosions in Granite.....	7
2. Hoggar Explosions.....	22
3. Results From Six Calculations.....	23
4. Explosive Test Series in Gas Fractured SWG.....	33

SECTION 1 INTRODUCTION AND SUMMARY

The purpose of this research program is to improve our understanding of explosion source functions and source coupling through theoretical modeling of underground explosions, and through laboratory modeling of explosions and theoretical simulations of the laboratory results. Simulation of underground explosions requires a detailed knowledge of material properties and constitutive models for the surrounding medium. Some of these properties are well constrained by observation, while others are much less certain. In this report, we summarize our current understanding of the constraints on modeling of underground nuclear explosions in granite.

S-CUBED has a history of very successful numerical modeling of explosion data (e.g. Rimer and Lie, 1982; Rimer and Cherry, 1983; Rimer and Lie, 1984). Near field data from the explosion PILEDRIVER, for example, has been quite accurately reproduced in both one- and two-dimensional calculations (Rimer et al., 1979; Day et al., 1983). In Section 2 of this report, we discuss the models that were used in these simulations, and show which of the aspects of the models are required by the data and which parameters are less well constrained. We then scale the PILEDRIVER results to correspond to the yields of HARDHAT and SHOAL and compare the results with near field waveforms from these events.

In Section 3, we discuss the effect of dilatancy introduced by the use of an associated flow rule in simulations of explosions in granite. The difference in cavity radii between the Hoggar explosions and NTS explosions could be explained if dilatancy were present in the Hoggar explosions, and absent in the NTS explosions. However, dilatancy would also severely change the ground motion. The ground motion in the dilatant Hoggar simulation is about a factor of three greater than the ground motion in the nondilatant NTS simulation. Dilatancy also has the effect of eliminating explosion spectral peaks. The large volume increase in the nonlinear zone near the explosion makes overshoot nearly impossible.

S-CUBED has the responsibility for planning and guidance of laboratory experiments now in progress at SRI and New England Research. Quasistatic tests are being done at New England Research to determine the material properties of the Sierra White Granite which is being used in the dynamic experiments at SRI. In Section 4, we report on the current status of these experiments.

SECTION 2

CONSTRAINTS ON MODELING OF UNDERGROUND EXPLOSIONS IN GRANITE

The parameters used in simulations of underground nuclear explosions are constrained by laboratory tests of material properties and by direct observations of ground motion from underground explosions. In this section we discuss the parameters and constitutive models that were used in S-CUBED granite calculations that successfully reproduced near-field waveforms and cavity radii, and examine the effect of changing these parameters.

Quasistatic laboratory tests are used to determine the following parameters: density, elastic moduli, pressure-volume relation, material strength, porosity, and water content. Of these quantities, the density, moduli, and P-V relation seem to be quite consistent with *in situ* rock properties. Porosity and water content are more variable *in situ* due to the presence of joints and are therefore less well constrained by laboratory data. Laboratory measurements of strength seem to be very inconsistent with *in situ* strength as inferred by modeling of underground explosions.

Direct observations of underground explosions provide some strong constraints on modeling. In particular, cavity radii measurements, near field observations of velocity and displacement, and in cases where full waveforms are not available (such as in the Hoggar explosions), peak displacement and peak velocity measurements all can be compared with the results of numerical simulations of underground explosions. The problem with using these observations for modeling is that the data quality is frequently inconsistent and uncertain. Also, unknown local variations in material properties add to the uncertainty of modeling the explosions. The dynamic experimental tests described in Section 4 are intended to be simulations of underground nuclear explosions. The reason for performing these tests is to try to reproduce the physics of underground explosions under more constrained conditions.

Complete near field time histories are available from three United States explosions in granite: PILEDRIVER, HARDHAT, and SHOAL (Table 1). We have digitized the near field data from these events for comparison with our calculations and for comparison with future experimental results. The PILEDRIVER data was collected by Sandia Laboratory¹ (Perret, 1968) and by Stanford Research Institute² (Hoffman and Sauer, 1969). The HARDHAT data was also collected by Sandia Corporation¹ (Perret, 1963), and by SRI (Swift and Eisler, 1962). The SHOAL data was collected by Sandia Corporation (Weart, 1965). Details of the experiments are given in a summary by Murphy (1978) as well as in these reports.

One- and two-dimensional calculations of PILEDRIVER performed earlier at S-CUBED were quite successful at modeling some of the near field data and reproducing the observed cavity radius (Rimer *et al.*, 1979; Day *et al.*, 1983). In addition to the horizontal data shown in this report, there is a substantial amount of vertical data available from PILEDRIVER, and this data was reproduced quite well in the two-dimensional calculations. The constitutive models used in these calculations are discussed in detail in Rimer *et al.* (1984). In Figures 1 and 2, we show a comparison of the observed near field velocity and displacement from PILEDRIVER compared with the results of one-dimensional calculation No. 570. The agreement between the calculated velocity and the data at the closest two stations is excellent. At the more distant stations, the shape of the velocity waveforms is reproduced by the calculation, but the amplitude of the waveforms is overestimated by about a factor of two. The more distant SRI stations are at a different azimuth than the closer Sandia stations, so the observed differences could be an indication of azimuthal variations of the near field waveforms. As shown in Table 1, the cavity radii from this calculation agree very well with the observed cavity radii (Heuze, 1983) for all three events.

In order to examine the amount of variation in these results, we scaled the PILEDRIVER calculation to the yield of the explosions HARDHAT and SHOAL and plotted the results together with near field observations for these events.

1. Now Sandia Laboratories

2. Now SRI International

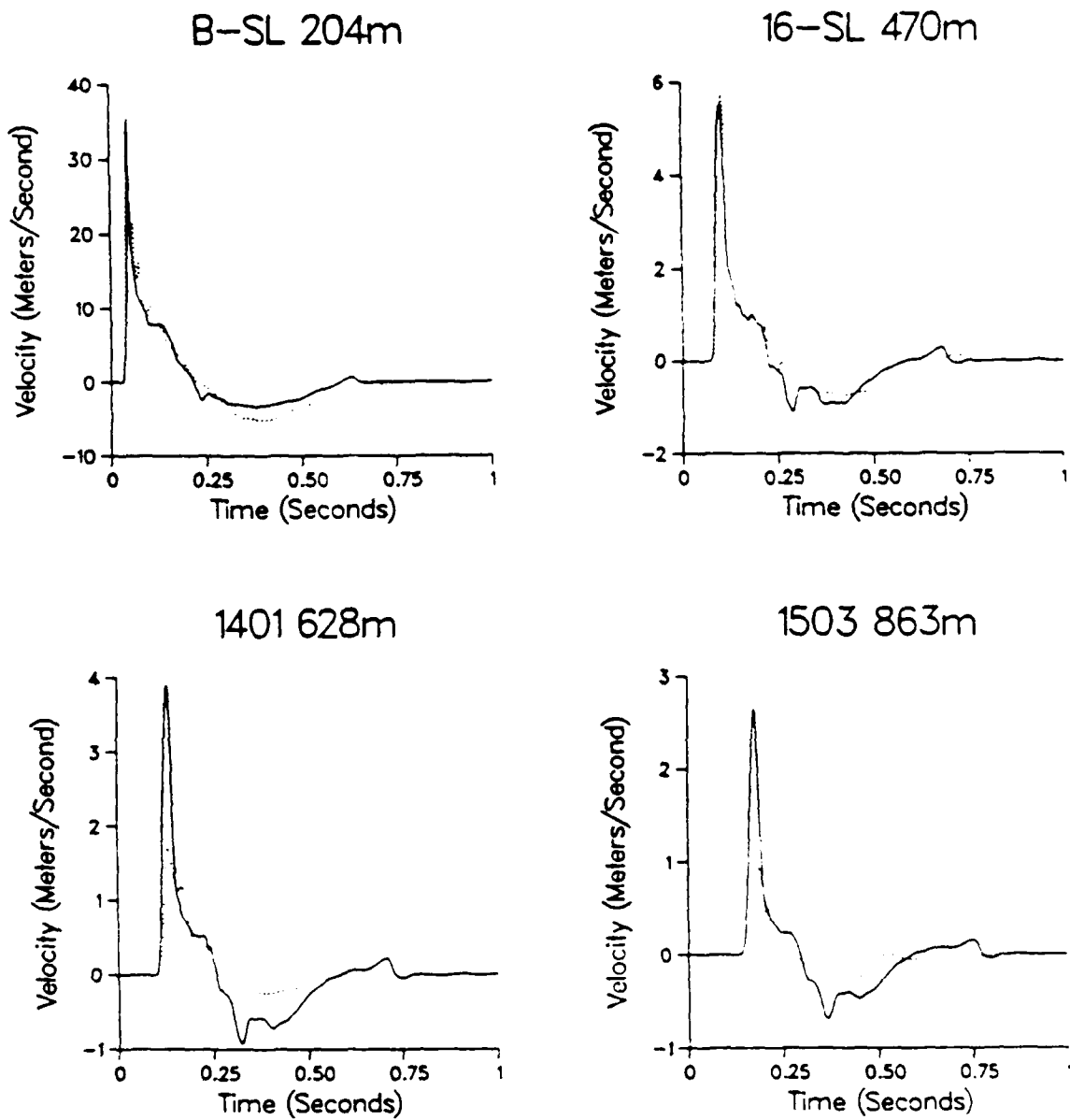


Figure 1. Near field velocity waveforms from PILEDRIVER compared to waveforms from calculation number 570. The solid lines are the calculated waveforms and the dotted lines are the data. The top two waveforms recorded 204 meters and 470 meters from the explosion are from Perret (1968) and the bottom two waveforms at 628 meters and 863 meters are from Hoffman and Sauer (1969).

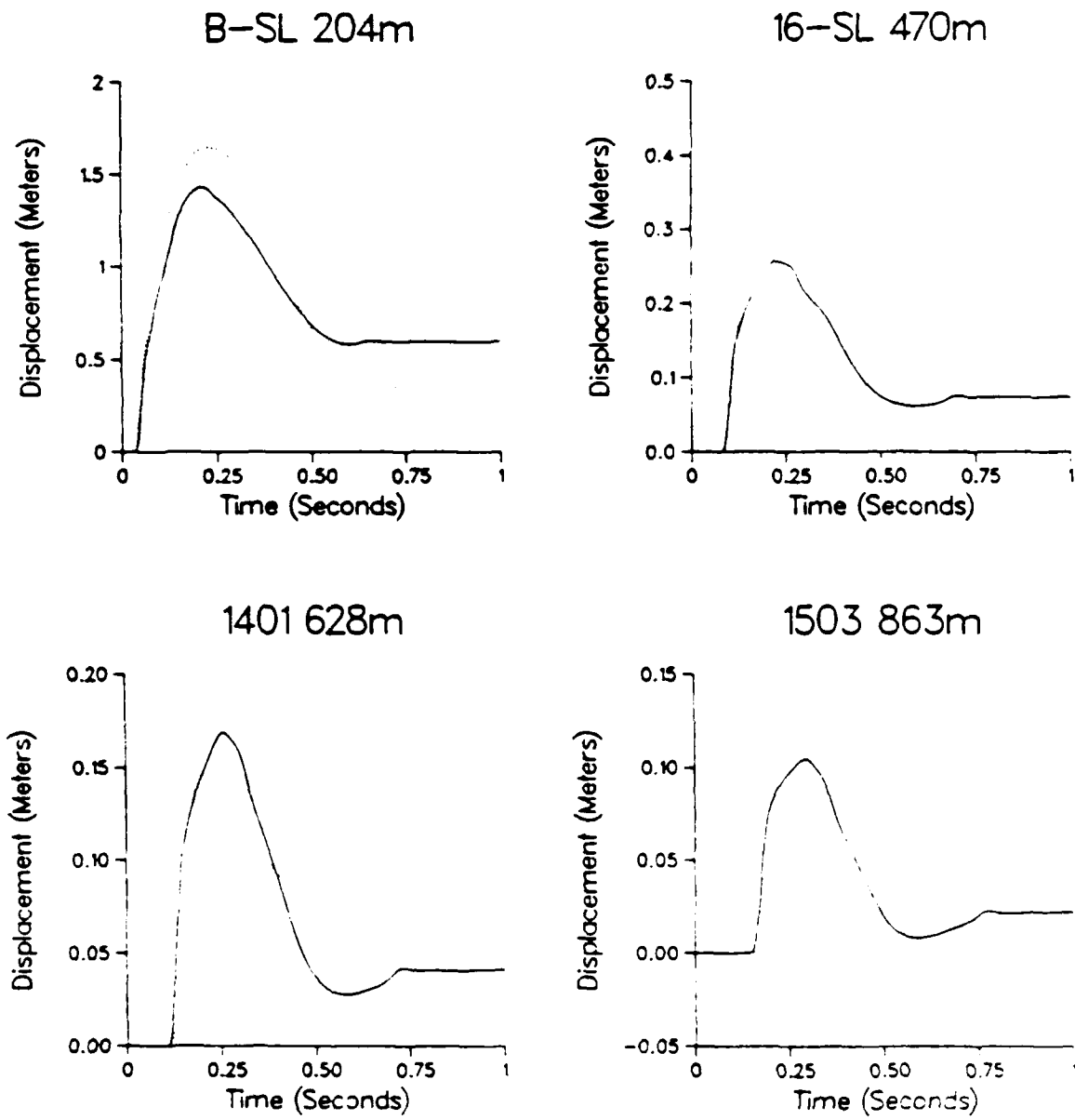


Figure 2. Observed near field displacement from PILEDRIVER compared to displacement from calculation number 570. The displacement data were obtained by integrating the velocity waveforms shown in Figure 1

TABLE 1
UNITED STATES EXPLOSIONS IN GRANITE

Explosion	Yield (KT)	Measured Cavity Radius (m)	Calculated (570) Cavity Radius (m)
PILEDRIVER	62.0	40.1/44.5*	42.5
HARDHAT	5.9	19.4	19.4
SHOAL	12.5	26.8	24.9

* 44.5 meters was reported in Heuze (1983). 40.1 meters was obtained by a drill back measurement (Sterrett, 1969).

HARDHAT was an earlier 5.9 kiloton explosion located very close to the PILEDRIVER site in the same medium as PILEDRIVER. The HARDHAT comparison is shown in Figures 3, 4 and 5. The results are similar to the comparison at the more distant PILEDRIVER stations. The HARDHAT peak velocity amplitudes are overestimated by about a factor of two at the Sandia stations and by about a factor of 1.5 at the SRI stations, however the calculated velocity pulses have the same shape as the data. In particular, as was the case with PILEDRIVER, the observed and calculated velocity waveforms are broad and have large negative velocities at late times. The HARDHAT displacement data at the SRI stations is matched very well by the calculation.

SHOAL was a 12.5 kiloton explosion in granite located away from the Nevada Test Site, so the material properties of the medium are not identical to those of PILEDRIVER and HARDHAT. The SHOAL comparison is shown in Figure 6. The results are similar to the HARDHAT comparison. Again the shape of the data is reproduced fairly well, but the calculation overestimates the amplitude of the velocity pulses. The SHOAL data illustrates one of the problems with such comparisons. Note that all three observations are at approximately the same range (in different directions), yet the observed velocity waveforms are quite different, especially at station PM-3. It is not clear whether the data is actually this nonisotropic, or whether there is some problem with the instrumentation that recorded the waveforms. However, as we remarked earlier, azimuthal variations were observed in both the PILEDRIVER data and the HARDHAT data as well.

Peak velocity and peak displacement data from explosions in granite are also available from the French nuclear explosions in the Hoggar (Heuze 1983). The Hoggar data and the peak velocity and peak displacement data from the United States granite tests are all plotted as a function of scaled distance (all data has been scaled to a yield of one kiloton) in Figures 7 and 8. The Hoggar near field data is quite consistent with near field data from the United States tests. Also shown on these figures are the scaled peak velocity and peak displacement curves from calculation number 570. The calculation is in good

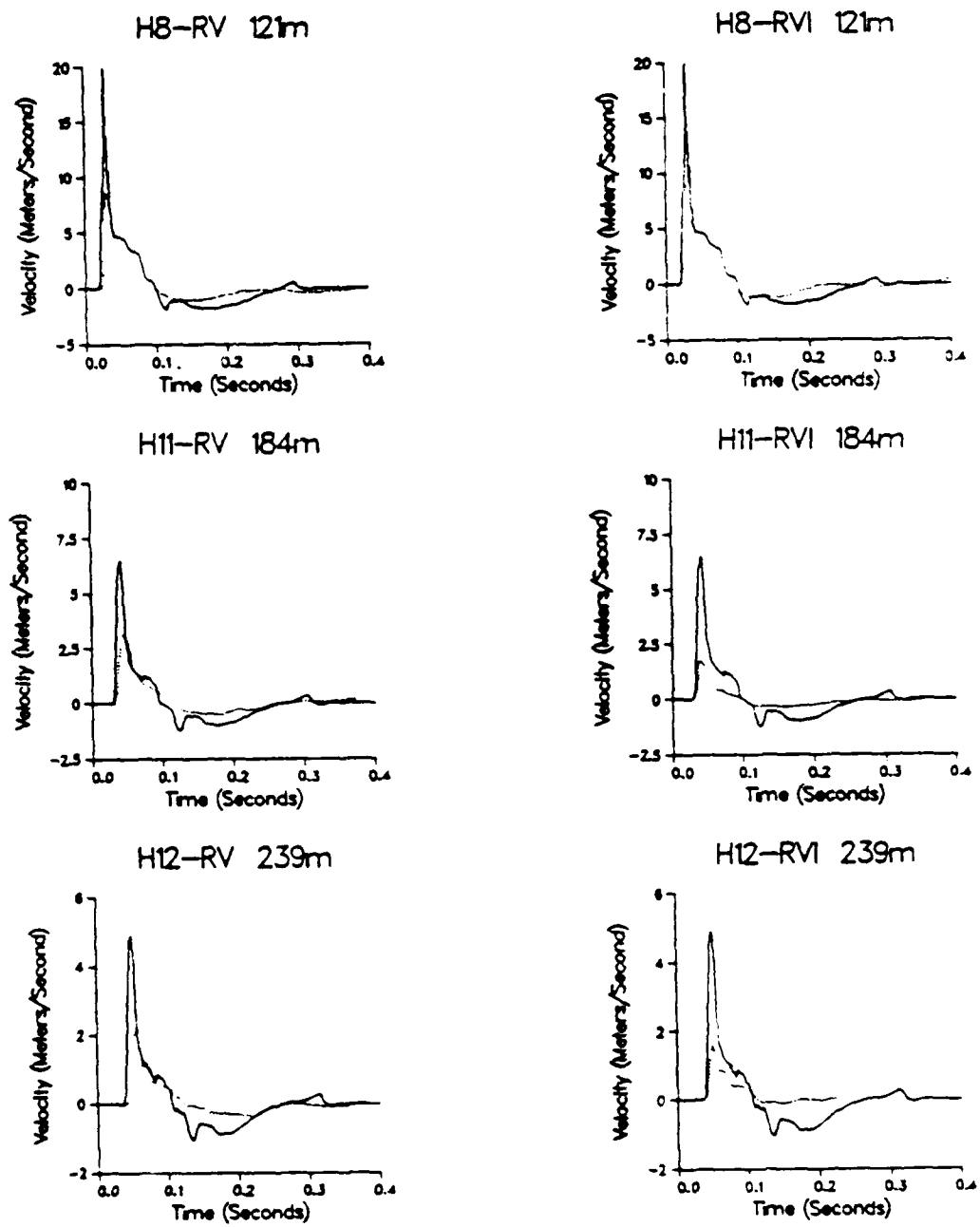


Figure 3. Near field velocity waveforms from HARDHAT compared to waveforms from calculation number 570 scaled to 5.9 kilotonns. The data is from Perret (1963). The data on the left are measured velocities, and the data on the right are integrated accelerations.

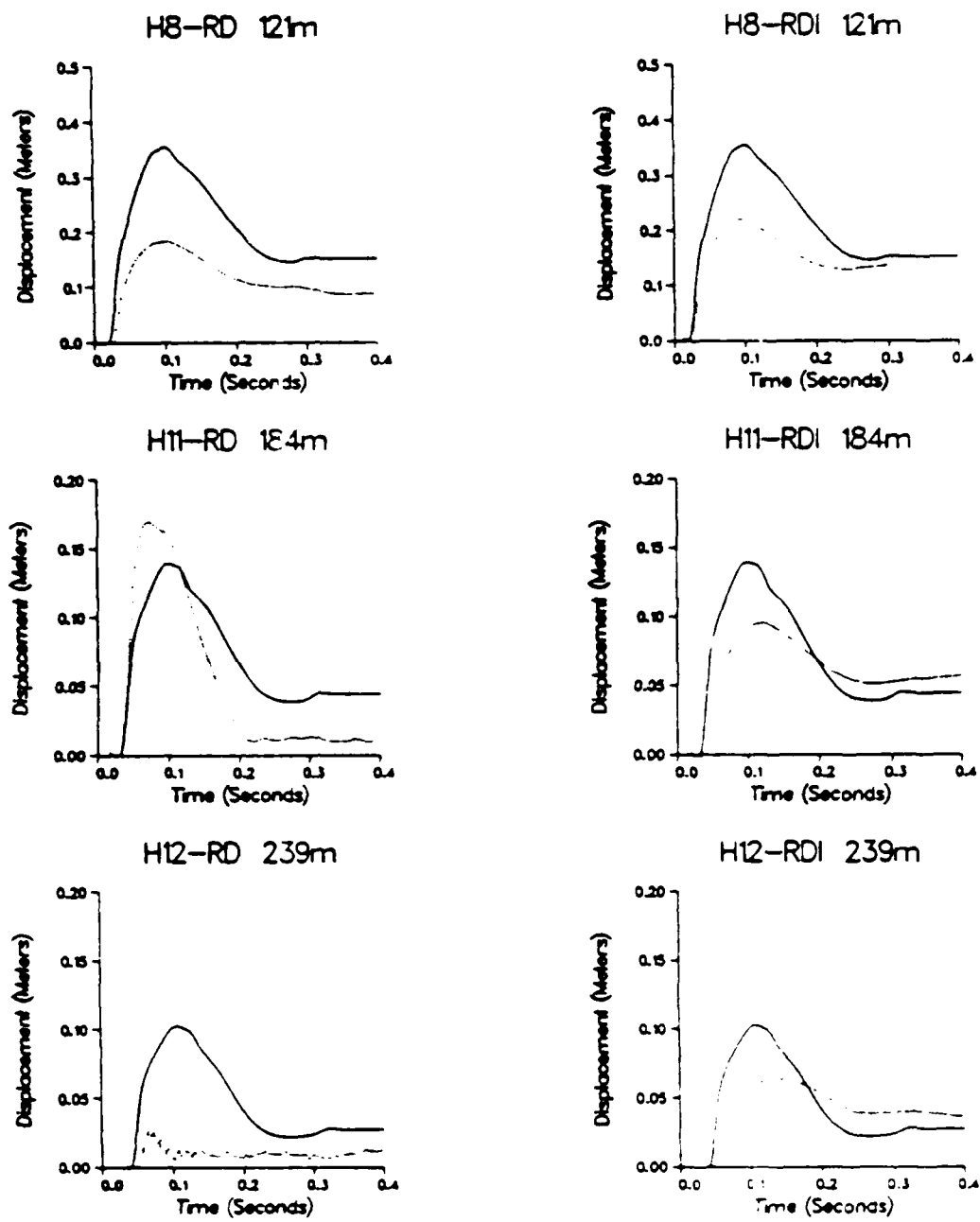


Figure 4. Near field displacement from HARDHAT compared to displacement from calculation number 570 scaled to 5.9 kilotonns. The data is from Perret (1963). The data on the left are measured displacements, and the data on the right are integrated velocities.

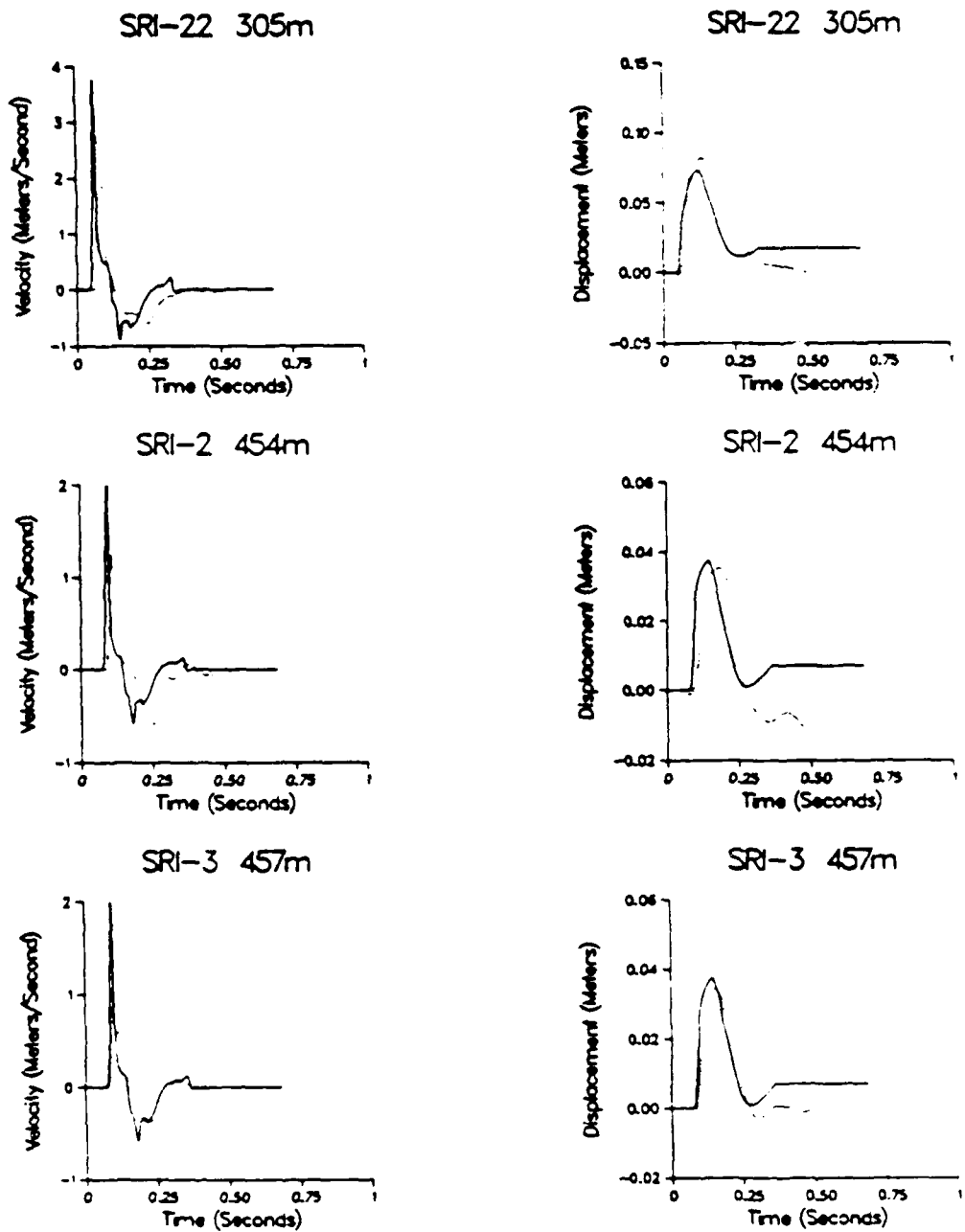


Figure 5 Near field velocity data (left) and displacement data (right) from HARDHAT compared to velocity and displacement from calculation number 570 scaled to 5.9 kilotons. The data is from Swift (1962). The displacements are integrated velocities.

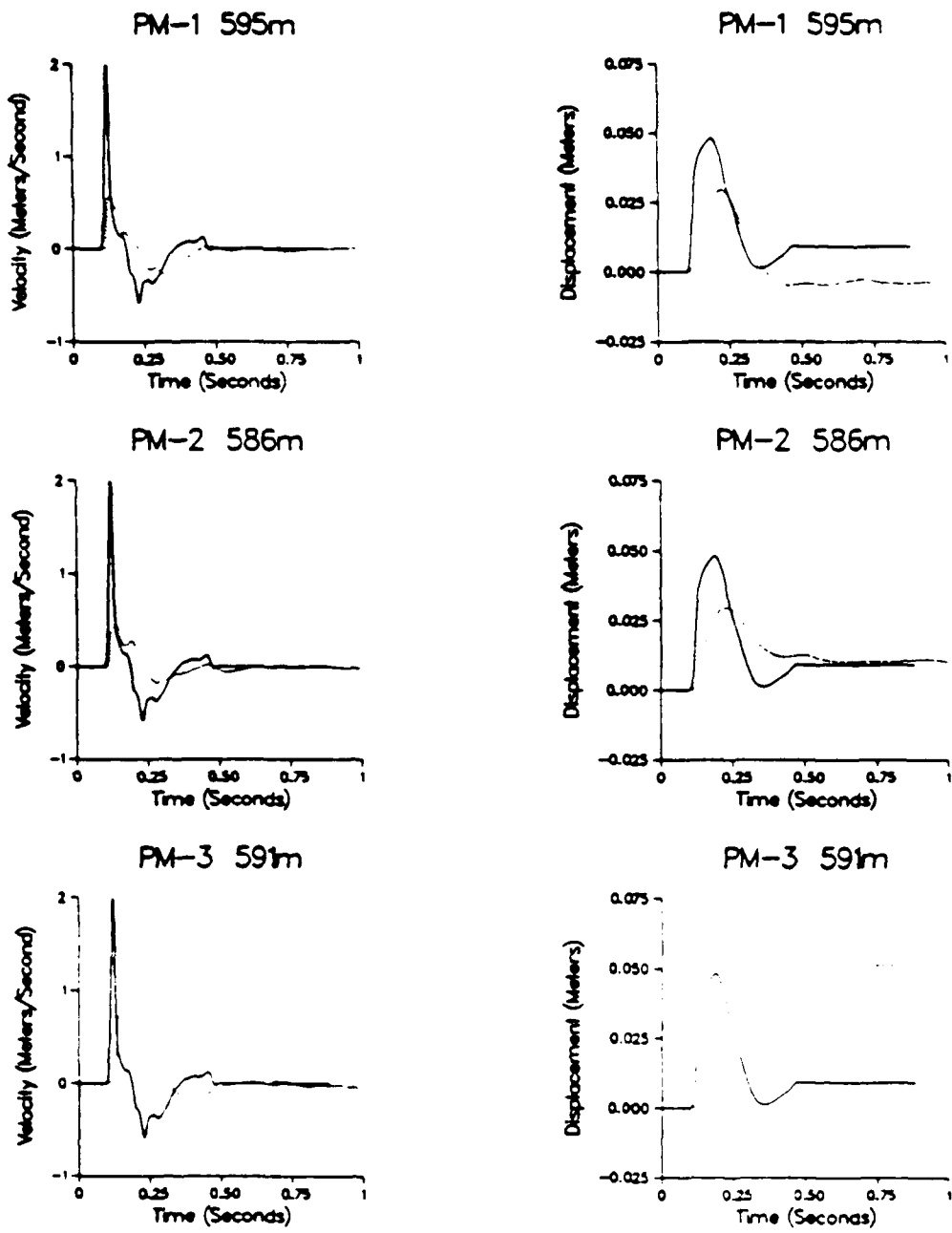


Figure 6. Near field velocity data (left) and displacement data (right) from SHOAL compared to velocity and displacement from calculation number 570 scaled to 12.5 kilotons. The data is from Weart (1965). The displacements are integrated velocities.

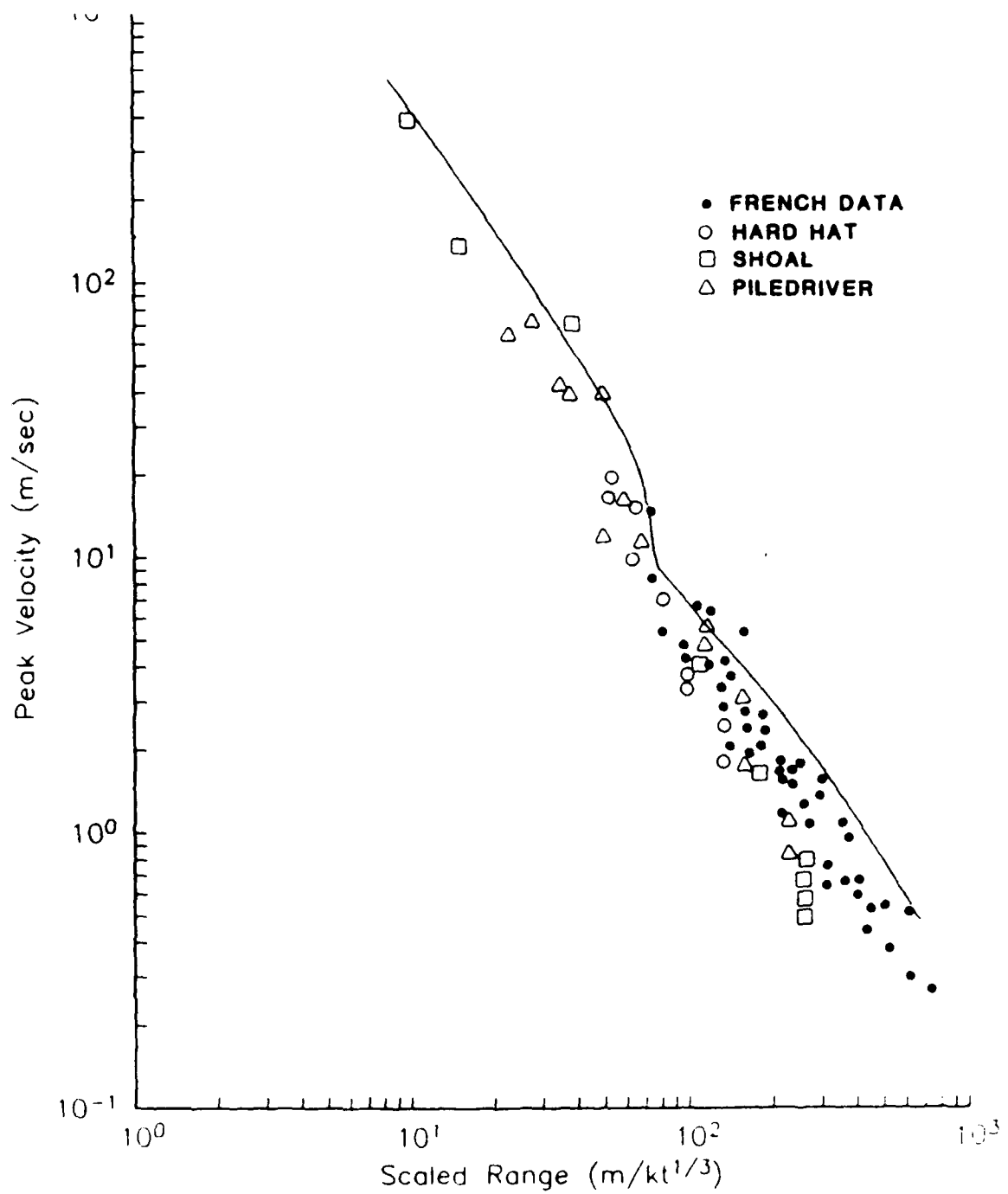


Figure 7 Peak velocity data from the Hoggar explosions and from the three United States Granite explosions all scaled to one kiloton plotted as a function of scaled range. The solid line is the peak velocity from calculation number 570

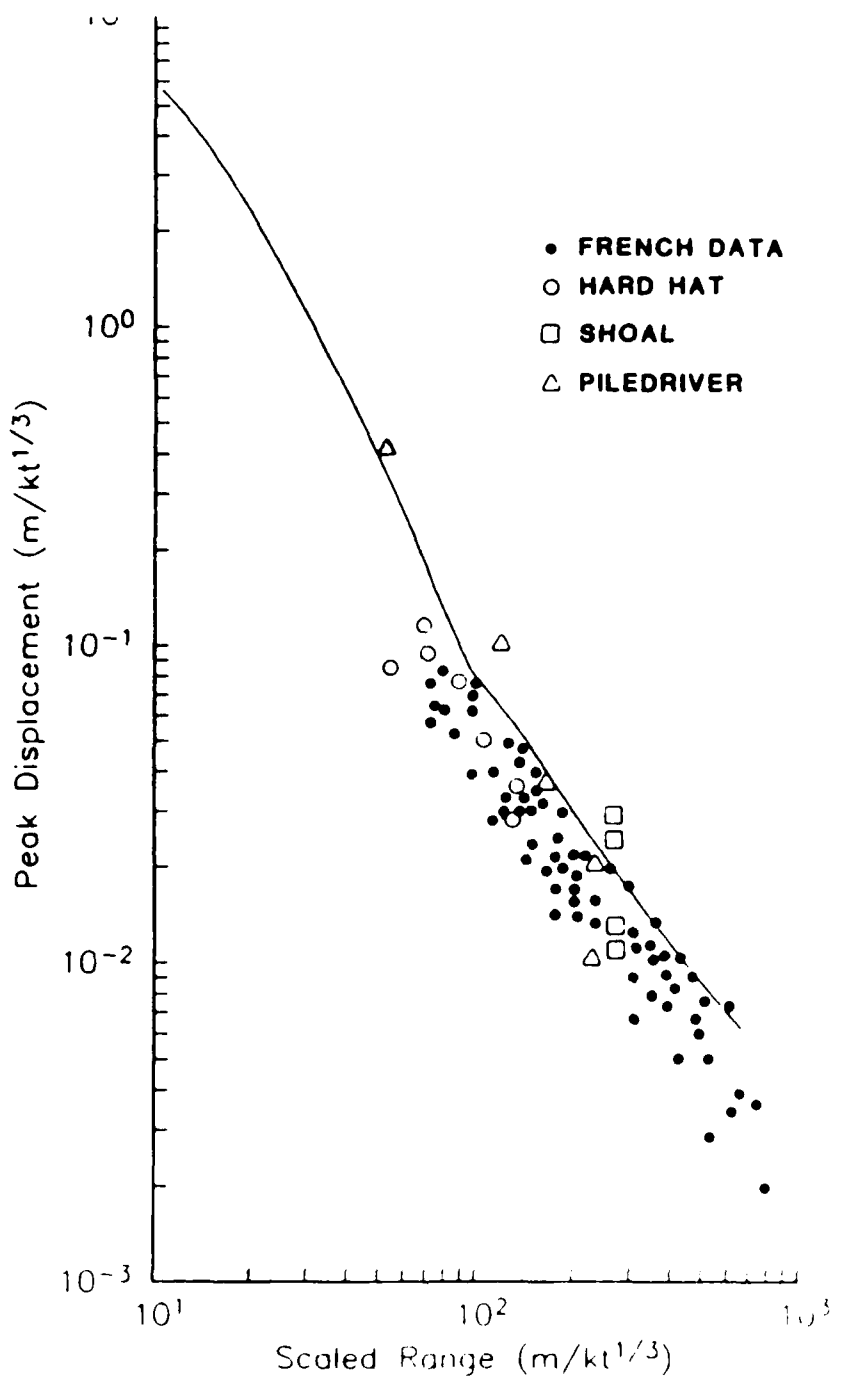


Figure 8 Peak displacement data from the Hoggar explosions and from the three United States Granite explosions all scaled to one kiloton plotted as a function of scaled range. The solid line is the peak displacement from calculation number 570

agreement with the data at close range, however as we saw in the waveform comparisons discussed earlier, the peak velocity and peak displacement data are lower than the calculation at larger ranges.

In the calculation (No. 570) discussed above, laboratory data was used to constrain the elastic moduli, density, and the initial strength of the rock (Cherry and Peterson, 1970). The failure surface used in the calculation is shown in Figure 9. The strength of the rock at \bar{P} equal to 0 is 150 bars. The strength was reduced during the calculation through the use of an effective stress law (e. g. Rimer et al., 1984). In this model, the medium starts out at the laboratory strength, but weakens as pores are crushed by the explosion. In porous materials, crushing of pores can have a very strong effect on source coupling, however the porosity of granite is very low (0.1 percent maximum porosity is used in the calculation), and the main effect of pore crushing is to trigger the strength reduction of the effective stress law.

The effect of this model is to severely weaken a zone around the explosion while leaving an intact high strength region farther out. As shown in Appendix A, a weakened core inside a strong rock matrix is necessary to generate the large overshoots and negative velocities that are observed in the data. It is well known that if laboratory strengths are used to simulate the near field data, the resulting waveforms are much too narrow, and low in amplitude (see Figures 10 and 11), and the resulting cavity radius is only about two-thirds of the observed cavity size. In Figures 12 and 13, we show the results of a calculation in which the medium is assumed to be very weak (200 bar failure surface) throughout the entire calculation. The resulting waveforms are a fair match to the data, however it does not reproduce the negative velocities at the closer stations, and the calculated cavity radius is overpredicted by about a factor of 3/2.

Either the effective stress law or some other mechanism for severely weakening the material near the explosion seems to be required to match both the near field data and the cavity radii. It is not clear why the calculations match some of the data very well, while overestimating the amplitudes at other stations. Some additional numerical modeling in conjunction with the experimental program could help to understand this data.

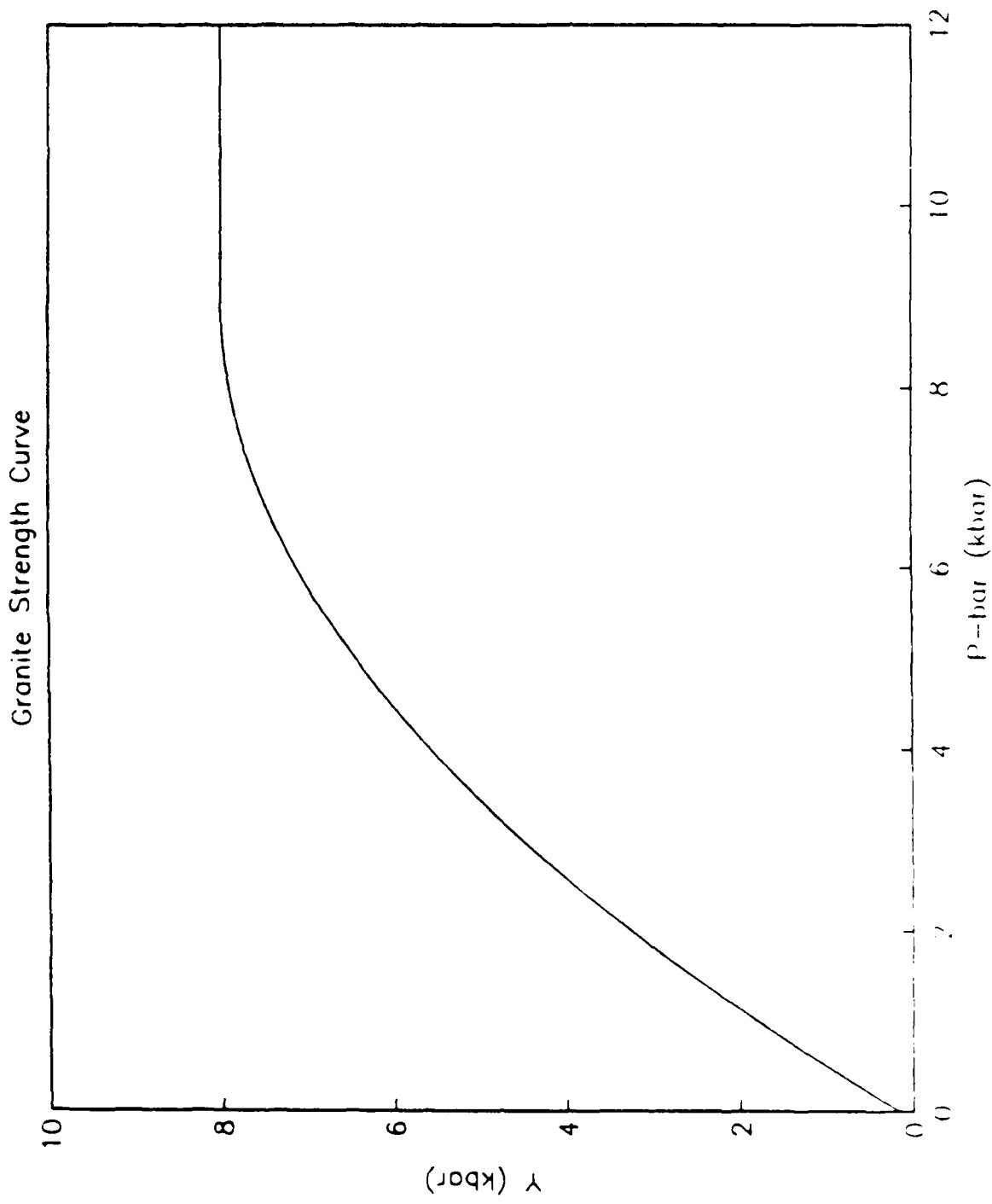
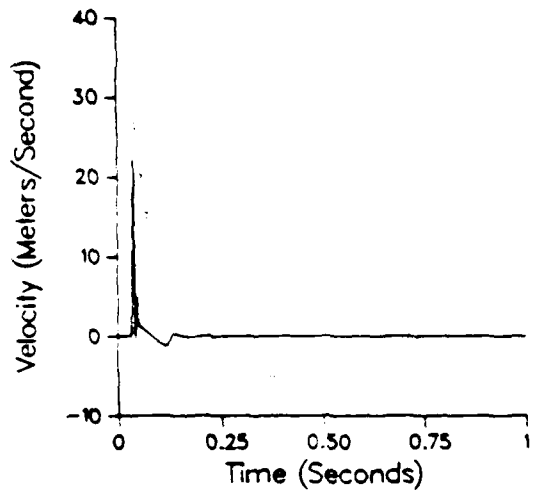
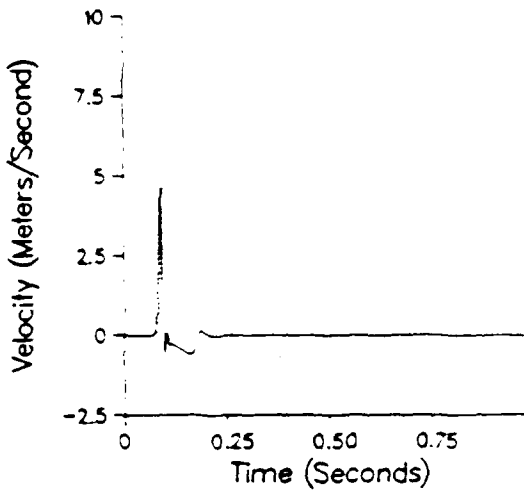


Figure 9 Failure surface used in calculations estimated from laboratory measurements of Climax Stock granite. In a spherically symmetric calculation γ is equal to the stress difference $|\sigma_{rr} - \sigma_{\theta\theta}|$, and p is equal to $1.2(\sigma_{rr} + \sigma_{\theta\theta})$. The failure surface is expressed in terms of γ and p so that the failure surface will be the same for failure in compression, extension, or torsion (Cherry and Pepperson 1970).

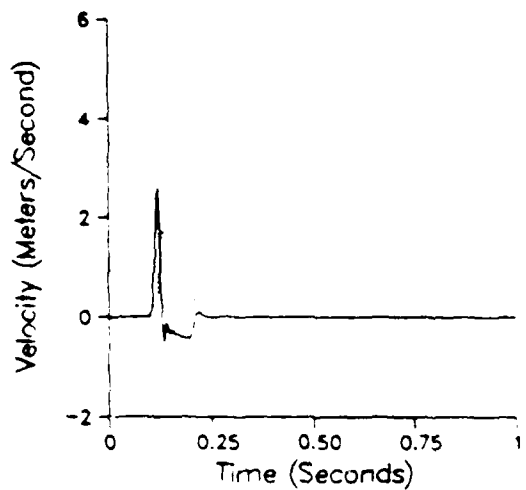
B-SL 204m



16-SL 470m



1401 628m



1503 863m

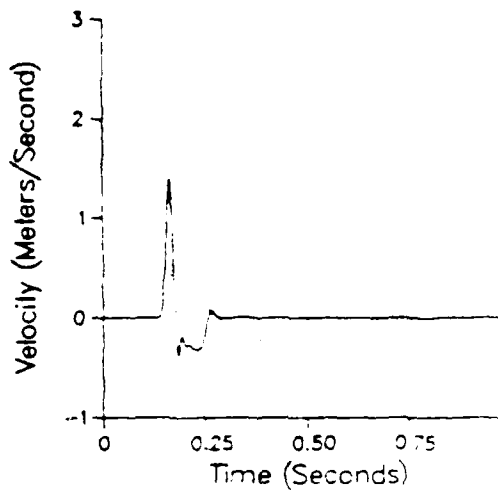
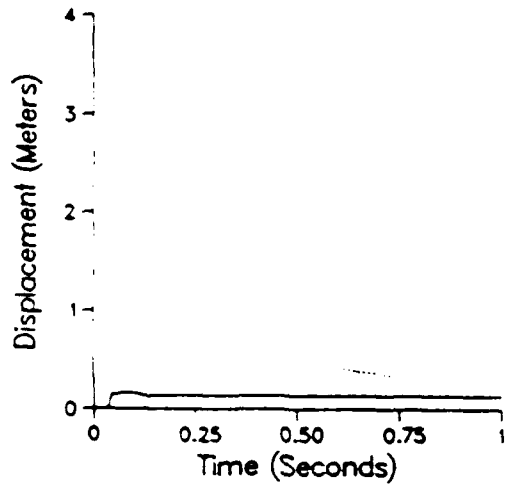
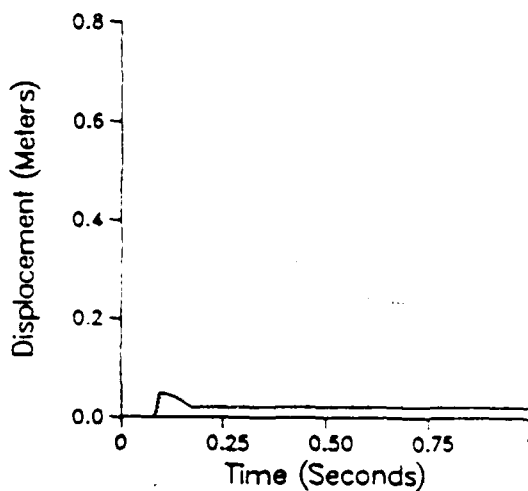


Figure 10. Near field velocity data from PILEDRIVER compared with data from a calculation using the laboratory strength of granite with no weakening.

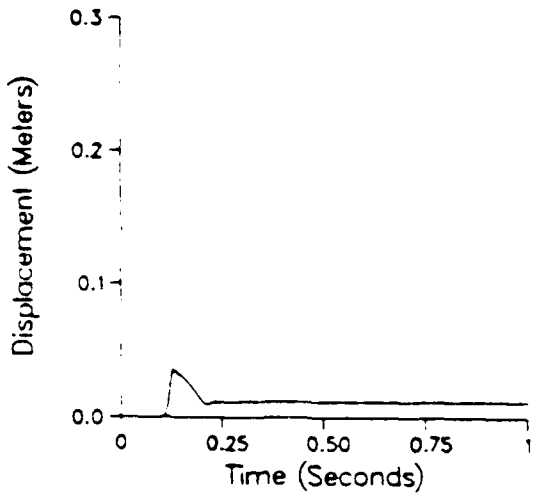
B-SL 204m



16-SL 470m



1401 628m



1503 863m

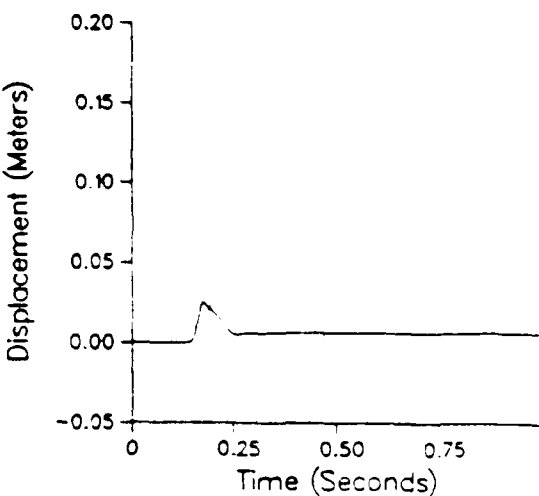
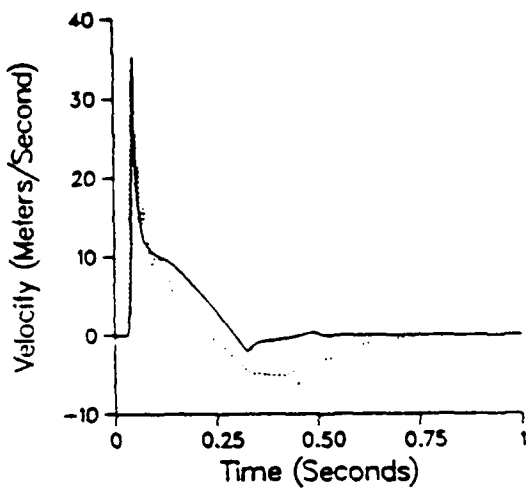
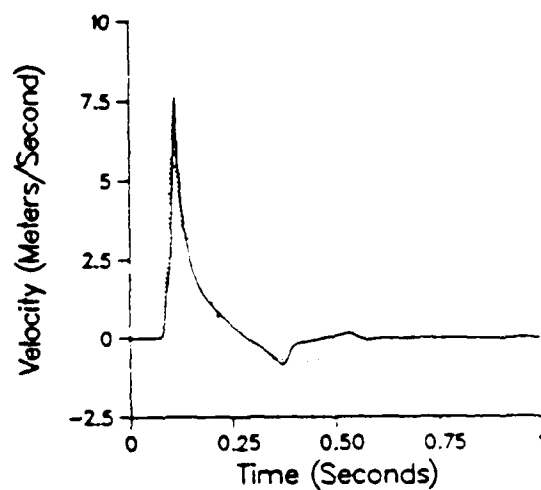


Figure 11 Near field displacement data from PILEDRIVER compared with data from a calculation using the laboratory strength of granite with no weakening.

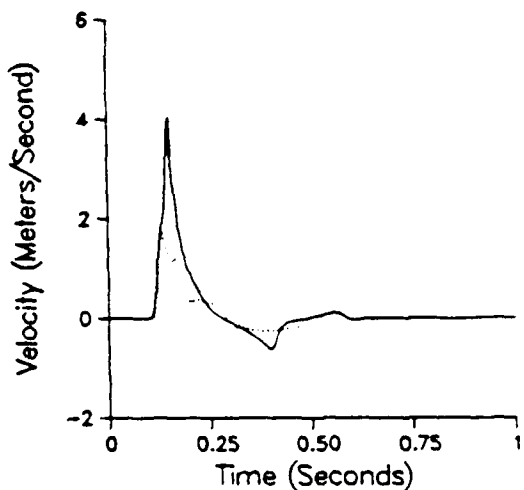
B-SL 204m



16-SL 470m



1401 628m



1503 863m

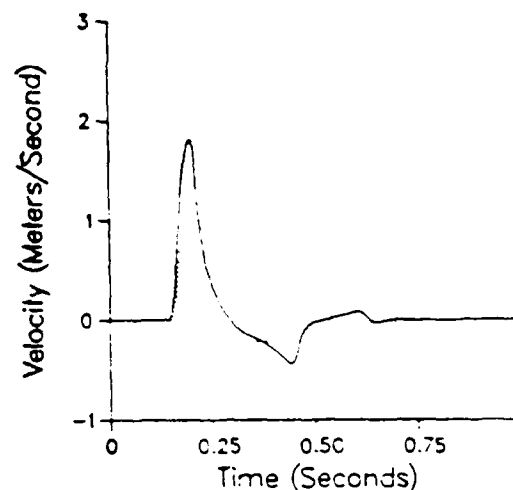
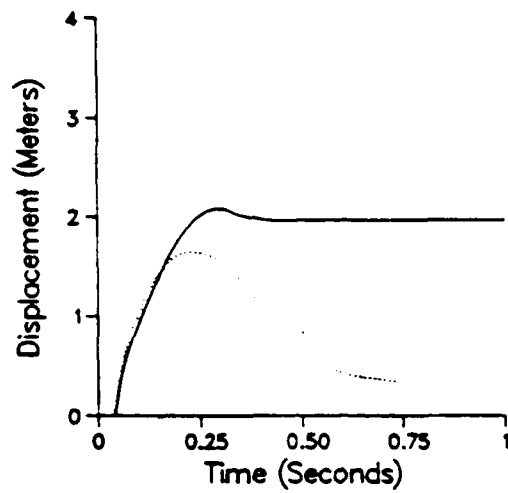
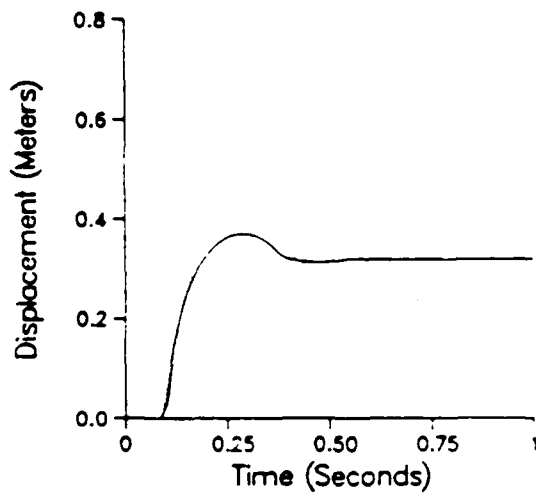


Figure 12. Near field velocity data from PILEDRIVER compared with data from a calculation using a strength of 200 bars throughout the calculation.

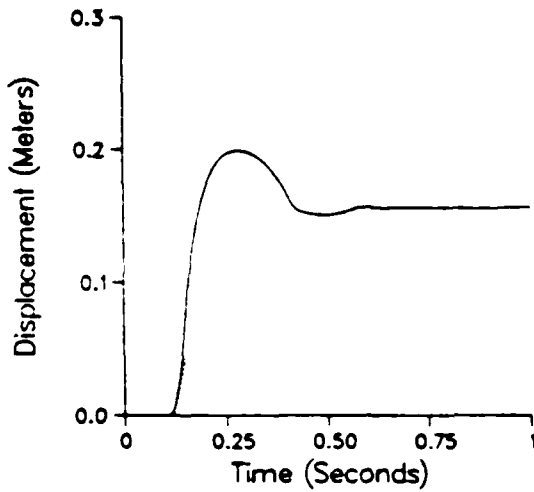
B-SL 204m



16-SL 470m



1401 628m



1503 863m

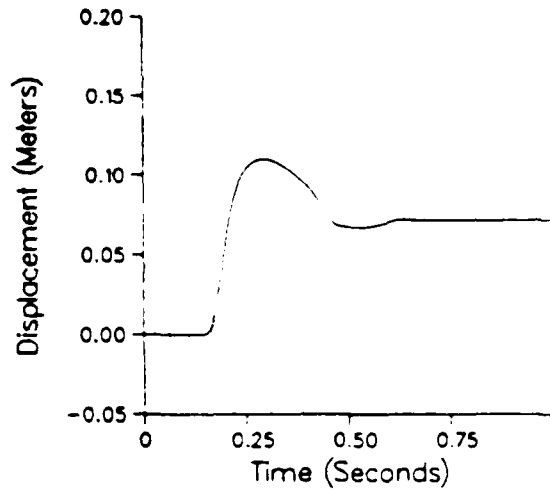


Figure 13. Near field displacement data from PILEDRIVER compared with data from a calculation using a strength of 200 bars throughout the calculation.

SECTION 3

THE EFFECT OF DILATANCY ON GROUND MOTION CALCULATIONS IN GRANITE

Most S-CUBED ground motion calculations have used a radial return nonassociated flow rule. In an earlier report (Rimer et al., 1986), we showed that using an associated flow rule to include dilatancy introduced by plastic flow caused significant changes in both cavity radii and ground motion. In this section we address the questions of how an associated flow rule affects the results of granite calculations, and whether dilatancy could explain the Hoggar/PILEDRIVER cavity size anomaly.

Information about four Hoggar explosions is listed in Table 2. When the measured cavity radii are cube root scaled to a yield of 62 kilotons, they are all about 30 meters, much less than the measured cavity radii for the three United States granite shots (Table 1) which all exceed 40 meters when scaled to 62 KT. Both the near field and far field data from the Hoggar explosions, however, are comparable in amplitude to the United States granite data. The reasons for this difference have not been explained, and we want to see if dilatancy could be responsible for this anomaly.

Dilatancy cannot be added directly to the calculation discussed in the last section, because the creation of a large volume of cracks induced by plastic flow is clearly incompatible with present models for pore crushing and the effective stress law. To examine the effect of dilatancy, we have done two sets of calculations. The results of these calculations are listed in Table 3. Figures showing near field waveforms, strain paths, and reduced displacement potentials from these calculations and the calculations described in the last section are in Appendix B. First, we ran the calculation with the high laboratory strength (see Figure 9) with an associated flow rule. The effect of the associated flow rule is largest when the slope of the failure surface is large, and there is no difference between an associated flow rule and a radial return flow rule when the

TABLE 2
HOGGAR EXPLOSIONS

Explosion	Yield	Measured Cavity Radius	Cavity Radius Scaled to 62 KT
GEORGETTE	13.0	17.0	28.6
MICHELE	3.6	10.2	26.3
MONIQUE	117.0	39.0	31.5
CARMEN	15.4	20.0	31.8

TABLE 3
RESULTS FROM SIX CALCULATIONS

Calculation	Cavity Radius (m)	Elastic Radius (m)	Ψ_{∞} (m ³)	Ψ_{\max} (m ³)
No. 570	42.5	600	16000	49000
200 Bar Strength	62.6	870	53000	57000
Laboratory Strength (Radial Return)	28.3	385	4700	5000
Laboratory Strength (Associated Flow Rule)	22.1	580	23000	23000
Slope 0.5 Failure Surface (Radial Return)	41.3	510	15000	15200
Slope 0.5 Failure Surface (Associated Flow Rule)	30.5	950	58000	58000

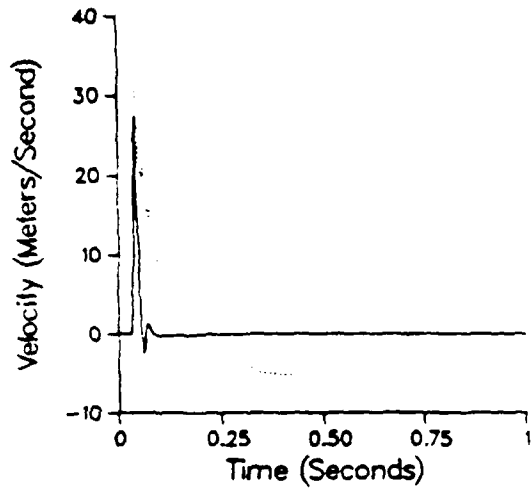
slope of the failure surface is zero. Because of this, dilatancy is small near the explosion because stresses are very high and failure occurs on or near the flat part of the failure surface. Dilatancy increases at greater distances where stresses are lower, and will also occur near the cavity at late times when stresses are reduced.

The effect of dilatancy is to slightly increase the pulse widths, to greatly increase the ground motion amplitude especially at larger ranges, and to reduce the cavity size. In Figures 14 and 15, we show a comparison between these results and the near-field PILEDRIVER data. The waveforms are much too narrow and are a poor match to the data. The cavity radius is also much smaller than the observed cavity radius. As expected, simply adding an associated flow rule to the laboratory data does not produce results consistent with the data

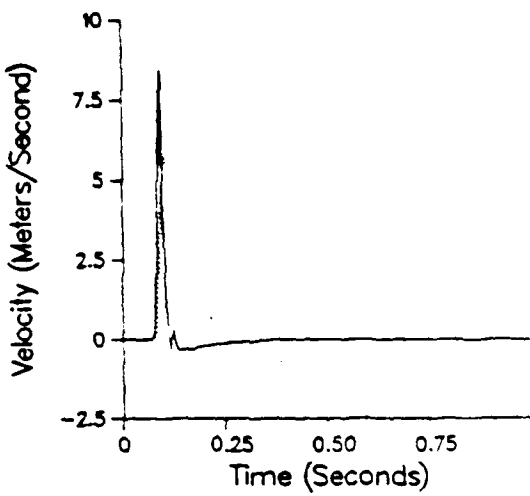
In the second set of calculations, we assumed a linear failure surface, and varied the slope and intercept of the curve, searching for the properties that would match the PILEDRIVER cavity radius and the (scaled) Hoggar cavity radius. The linear failure surface leads to more dilatancy than the quadratic failure surface used above, because the slope of the linear failure surface is steeper at higher stresses. Each calculation was run twice, once using a radial return flow rule and once using an associated flow rule. With a failure surface slope of 0.5, an intercept at zero pressure of 125 bars, and a maximum strength of 10 kilobars, the calculation with the radial return flow rule matches the cavity radius of PILEDRIVER, and the calculation with the associated flow rule matches the cavity radius of the Hoggar explosions. The ground motion in the dilatant calculation (velocity, displacement, and RDP) is approximately three times as large as the ground motion of the nondilatant calculation.

The fact that we can match both the Hoggar and PILEDRIVER cavity radii is interesting, but it is not clear that it has any relation to reality. The observed ground motion from the Hoggar explosions was comparable to that from PILEDRIVER (Heuze, 1983), while the calculations show that dilatancy would cause much larger ground motion. The waveforms in both calculations

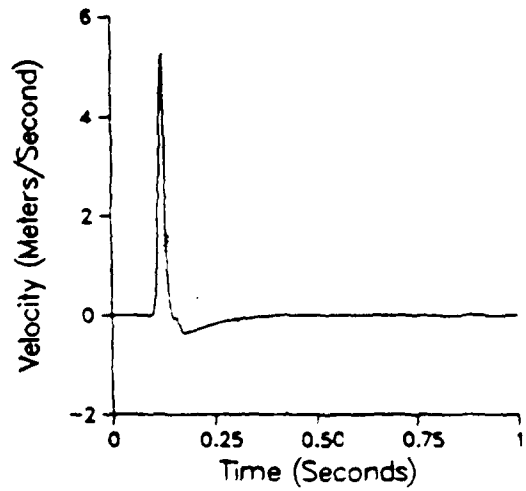
B-SL 204m



16-SL 470m



1401 628m



1503 863m

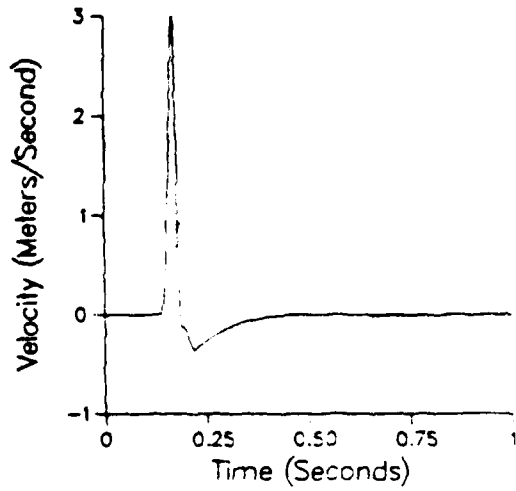
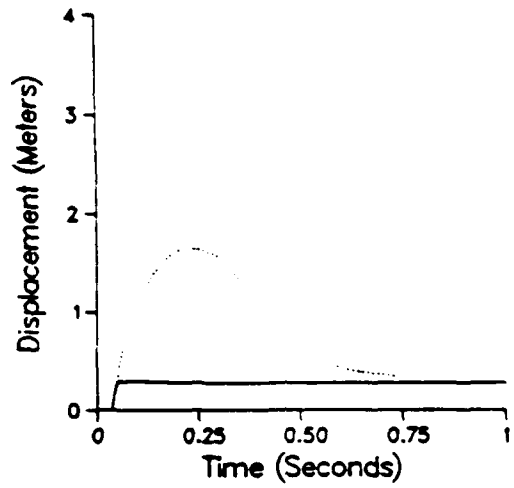
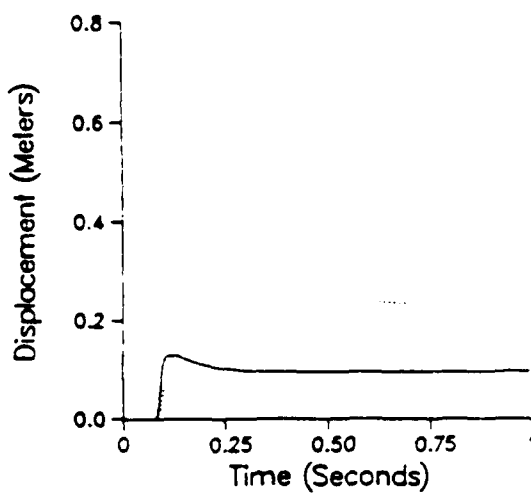


Figure 14. Near field velocity data from PILEDRIVER compared with data from a calculation using the laboratory strength of granite and an associated flow rule

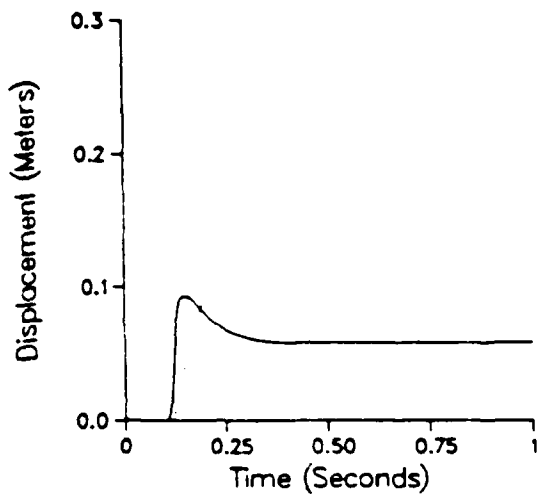
B-SL 204m



16-SL 470m



1401 628m



1503 863m

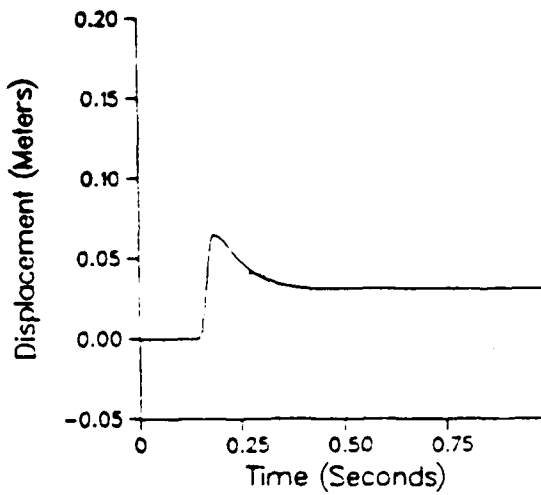


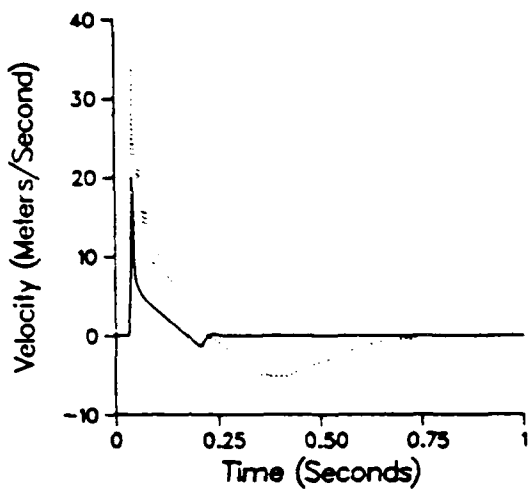
Figure 15

Near field displacement data from PILEDRIVER compared with data from a calculation using the laboratory strength of granite and an associated flow rule

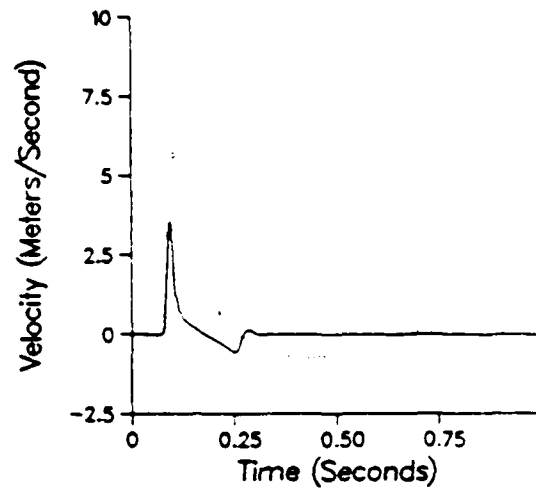
are a poor match to the near field PILEDRIVER ground motion (Figures 16 through 19). It is unfortunate that there are no near field ground motion records available from any of the Hoggar explosions. The added crack volume induced by the associated flow rule makes overshoot almost impossible. As a result, the large negative velocities observed near PILEDRIVER and the other NTS granite events cannot be modeled with an associated flow rule.

In Table 3, we list the peak RDP value and the final RDP value for each of the calculations (figures of the RDP and RVP for each calculation are in Appendix B). In all of the calculations without a weakened core, there is very little overshoot (see Appendix A for a theoretical discussion of the relation between the weakened core and overshoot). The effect of dilatancy is to increase the amplitude of the RDP while inhibiting overshoot even further. Since the increase in amplitude is true at all frequencies, an explosion that generated the amount of dilatancy predicted by the associated flow rule would generate both very large body waves and very large surface waves compared to an explosion that did not produce a dilatant region.

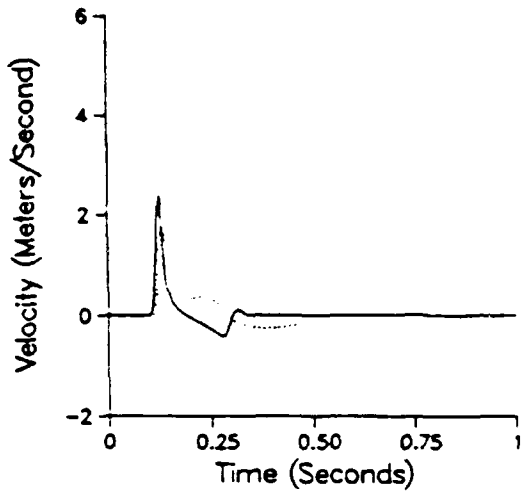
B-SL 204m



16-SL 470m



1401 628m



1503 863m

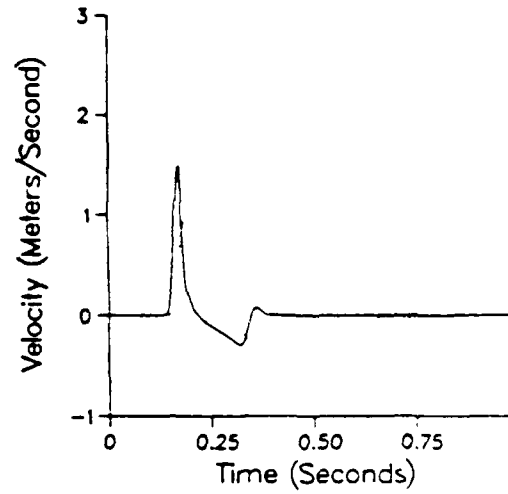


Figure 16. Near field velocity data from PILEDRIVER compared with data from a calculation using a failure surface with a slope of 0.5 and a radial return flow rule.

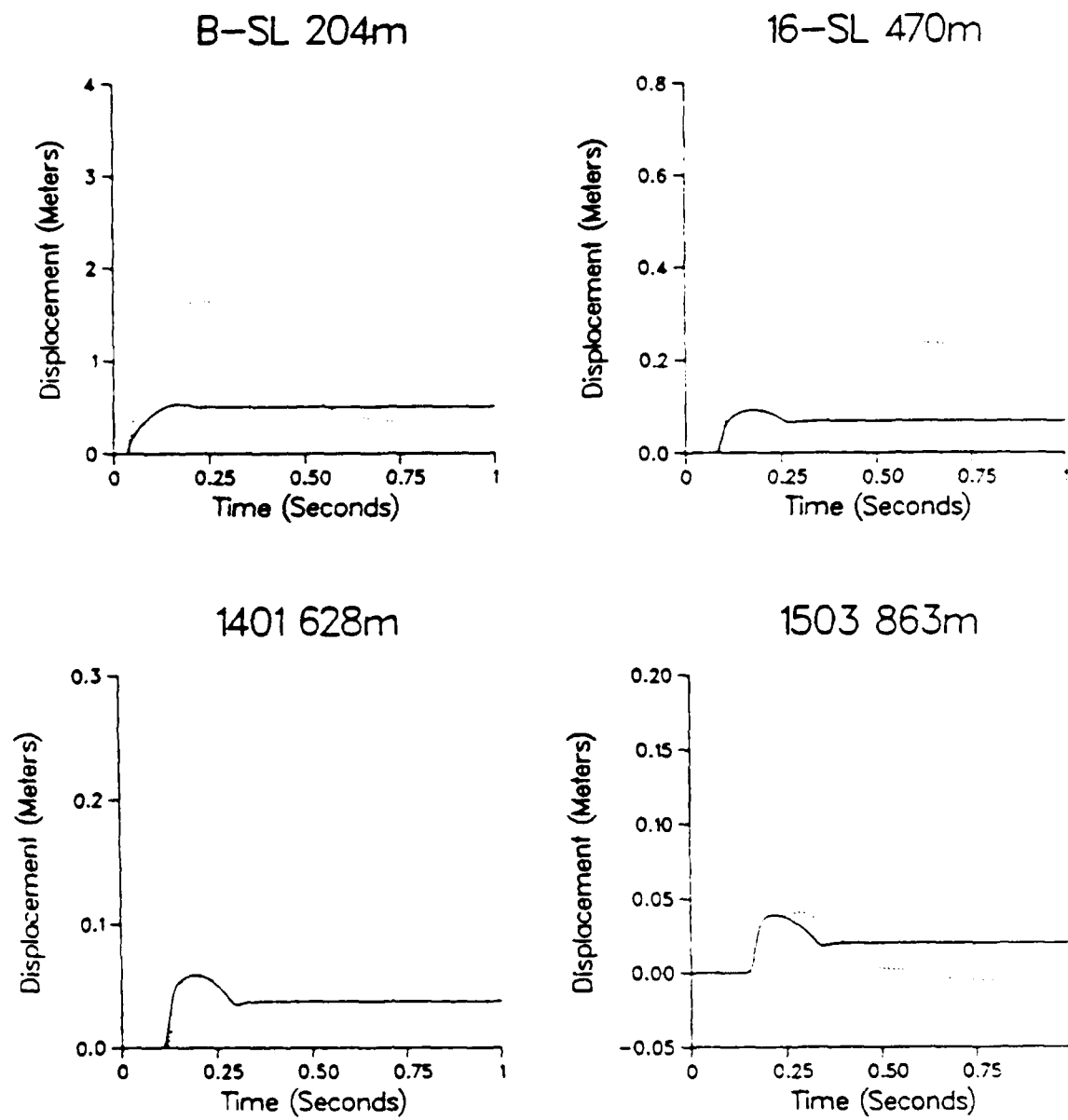
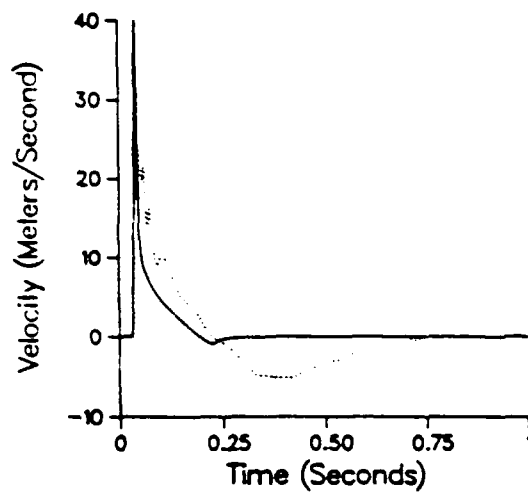
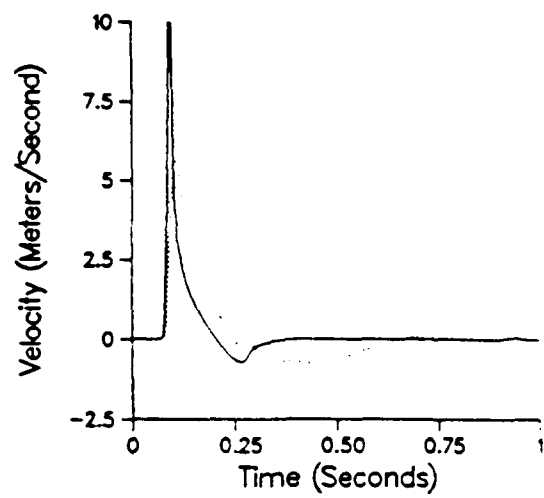


Figure 17. Near field displacement data from PILEDRIVER compared with data from a calculation using a failure surface with a slope of 0.5 and a radial return flow rule

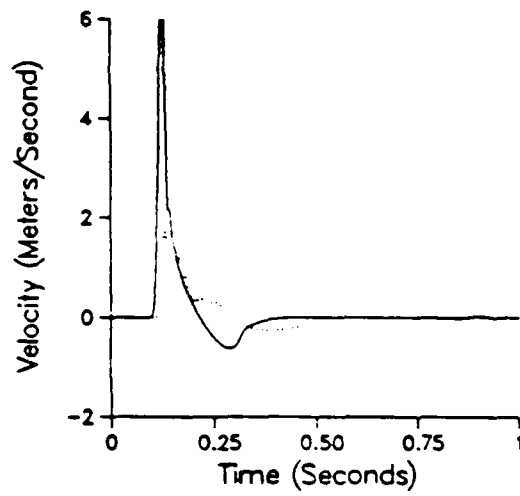
B-SL 204m



16-SL 470m



1401 628m



1503 863m

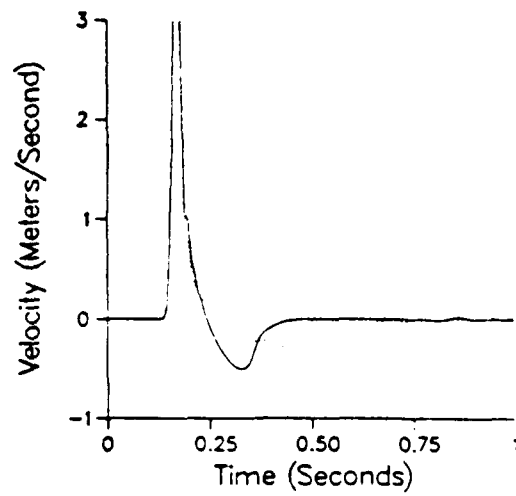
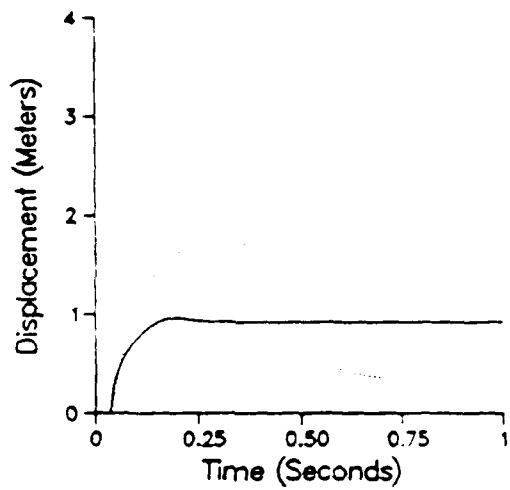
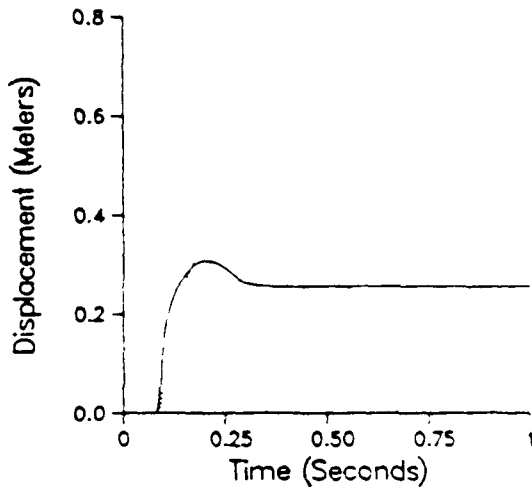


Figure 18. Near field velocity data from PILEDRIVER compared with data from a calculation using a failure surface with a slope of 0.5 and an associated flow rule.

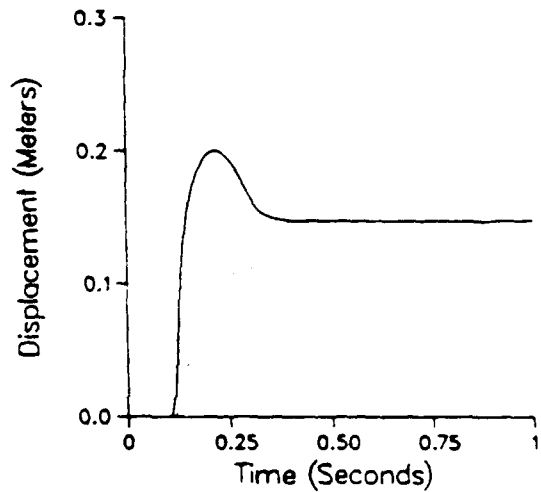
B-SL 204m



16-SL 470m



1401 628m



1503 863m

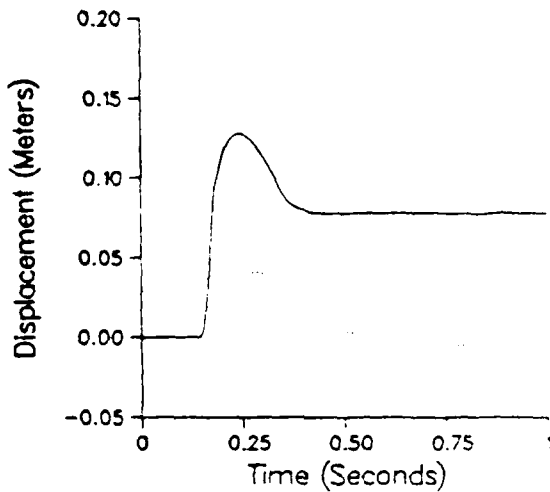


Figure 19 Near field displacement data from PILEDRIVER compared with data from a calculation using a failure surface with a slope of 0.5 and an associated flow rule

SECTION 4

STATUS OF LABORATORY EXPERIMENTS

As described in Section 2, laboratory quasistatic material properties measurements on granite samples show a much larger strength than that needed to simulate the PILEDRIVER particle velocity measurements. The strength reduction required to simulate these ground motion measurements was assumed to be due to pore pressure buildup which was modeled by Rimer, et al., 1984 using an effective stress law. However, other mechanisms for strength reduction are possible. The small scale explosive experiments being conducted at SRI International in Sierra White Granite (SWG) are intended to isolate the physical basis for the near field ground motion measurements from the PILEDRIVER event in NTS granite. As described by Nagy and Florence, 1986, the most recent series of SRI explosive tests did show a factor of three increase in particle velocity pulse widths for granite test samples which were extensively gas fractured and then water saturated. Less fractured samples in earlier tests did not show these increases in pulse widths when saturated, nor did gas fractured dry samples. The more fractured laboratory test samples are intended to more closely simulate "in a scaled sense" the *in situ* fractured and jointed rock.

As described in Rimer, et al., 1986, major problems exist in interpreting the experimental results, in particular the small cavity radii which appear to be inconsistent with the velocity measurements, and the lack of rebound implied by some of the particle velocity measurements. It is also clear that the two halves of the cylindrical test samples had separated for a time allowing HE detonation products to vent along the plane of the particle velocity gauges and sweep the closest in gauges out of their emplacement grooves. Recommendations were made which should improve the quality of the explosive tests being conducted this year at SRI. Table 4 (from Rimer, et al., 1986) summarizes the recommended explosive test series. Numbered tests indicate experiments completed in Fiscal Year 1986.

TABLE 4
EXPLOSIVE TEST SERIES IN GAS FRACTURED SWG.

Test Type ^a	Pore Condition	Overburden Pressure bars	(psi)	Pore Pressure bars	(psi)
1 (473, 474) ^b	Fully Saturated	136	(2000)	136	(2000)
2 (476) ^c	Vacuum Dried	136	(2000)	0	(0)
3 ^d	Fully Saturated	136	(2000)	3	(50)
4	Fully Saturated	68	(1000)	3	(50)
5	Vacuum Dried	68	(1000)	0	(0)
6	Fully Saturated	136	(2000)	68	(1000)

- a. Two tests are recommended for each test type.
- b. Fully saturated tests were actually conducted with a vertical confining (clamping) pressure of 136 bars but hydrostatic overburden and pore pressures of 122 bars for Test 473 and 109 bars for Test 474.
- c. Test 476 did not have complete data recovery.
- d. A nominal pore pressure of a few bars is simpler experimentally than zero pore pressure

The extensive gas fracturing of these SWG samples clearly alter their material properties. Therefore a series of quasistatic material property tests were also recommended by Rimer, et al. (1986). These included uniaxial strain load-unload, triaxial compression, and load-unload tests along strain paths relevant to the SRI experiments. The material properties tests are being conducted by Dr. Randolph Martin of the New England Research Corporation. On August 18, 1986, a meeting was held at SRI, with S-CUBED, SRI and New England Research Corporation represented, to coordinate the material properties tests with the dynamic explosive experiments so that maximum return is achieved from the limited funds available.

Granite samples fractured at SRI have already been received by New England Research and Dr. Martin anticipates completion of the first phase of the material properties tests by the end of October. SRI has recently completed the first particle velocity experiment of this new test series. This experiment, Test 485, was a repeat of dry Test 476 with deeper grooves for all the particle velocity gauge wires, including comparisons at the direct ranges between these grooves and still deeper grooves on the other half of the cylindrical SWG specimen. The sample halves again separated during the experiment but gauges remained in the grooves and survived. The deepest grooves gave the cleanest records. Peak displacements and cavity size agreed well with Test 476 data where available and filled in the gaps in these data.

Based upon this successful experiment, SRI will next execute a fully saturated experiment with very low pore pressure. Upon completion of this experiment and the first phase of the quasistatic experiments, another meeting will be held at SRI with S-CUBED, SRI and New England Research Corporation representatives present to analyze results before proceeding with the remaining experiments.

SECTION 5 REFERENCES

Cherry, J. T. and F. L. Peterson (1970). "Numerical Simulation of Stress Wave Propagation from Underground Nuclear Explosions," in *Engineering With Nuclear Explosives, 1*, Available from Clearing House for Federal Scientific and Technical Information, National Bureau of Standards, Springfield, Virginia.

Day, S. M., N. Rimer and J. T. Cherry (1983). "Surface Waves from Underground Explosions with Spall: Analysis of Elastic and Nonlinear Source Models," *BSSA*, 73, pp. 247-264.

Heuze, F. E. (1983). "A Review of Geomechanics Data from French Nuclear Explosions in the HOGGAR Granite. With Some Comparisons to Tests in U. S. Granite," Lawrence Livermore National Laboratory Report UCID 19812, May.

Hoffman, H. V. and F. M. Sauer (1969). "Free Field and Surface Motions. PILEDRIVER Event," Stanford Research Institute Report, POR-4000.

Murphy, J. R. (1978). "A Review of Available Free-Field Seismic Data from Underground Nuclear Explosions in Salt and Granite," Computer Sciences Corporation Report CSC-TR-78-0003.

Perrett, W. R. (1963). "Shot Hard Hat: Free-Field Ground Motion Studies in Granite," Sandia Corporation Report POR-1803.

Perrett, W. R. (1968). "Free Field Ground Motion in Granite. PILEDRIVER Event," Sandia Laboratory report, POR-4001.

Rimer, N. and J. T. Cherry (1983). "Verification of TTBT Calibration Yields" S-CUBED Final Report Task 3. Near Site Characteristics submitted to the Air Force Office of Scientific Research, SSS-R-83-6254, August.

Rimer, N., S. M. Day, G. A. Hegemier, H. E. Read, S. K. Garg and S. Peyton (1984). "Effect of Pore Fluid Pressure on Explosive Ground Motions in Low Porosity Brittle Rocks," S-CUBED Final Report SSS-R-84-6766, submitted to the Defense Nuclear Agency, DNA-TR-85-245, July

Rimer, N. and K. H. Lie (1982), "Numerical Simulation of the Velocity Records from the SRI Grout Spheres Experiments," S-CUBED Topical Report, SSS-R-82-5580, submitted to the Defense Nuclear Agency, DNA-TR-82-54.

Rimer, N. and K. H. Lie (1984), "Numerical Predictions of the Ground Motions from a ONE-TON In Situ High Explosive Event in Nevada Test Site Tuff," S-CUBED Topical Report SSS-R-84-6493, submitted to the Defense Nuclear Agency.

Rimer, N., J. L. Stevens and K. H. Lie (1986), "Effects of Pore Pressure and Fractures on Ground Motion in Granite," S-CUBED Final Report SSS-R-86-7974 submitted to the Defense Nuclear Agency, DNA-TR-86-227, June.

Sterret, T. S. (1969), "Drilling Investigation of the Lower Part of the PILEDRIVER Cavity," Lawrence Livermore Laboratory Report, UCRL-50765.

Swift, L. M. and J. D. Eisler (1962), "Nougat Series, ANTLER and HARD HAT Events, Measurement of Close-In Earth Motion," Stanford Research Institute Report, VUF-2100.

Weart, W. D. (1965), "Project Shoal: Free Field Earth Motion and Spalling Measurements in Granite," Sandia Corporation Report VUF-2001, February.

APPENDIX A

SOME ANALYTIC RESULTS RELEVANT TO SHOCK WEAKENING IN GRANITE

The explosion source function (i.e., the moment function $m(t)$, or equivalently, the reduced displacement potential $\psi(x)$) can be related to source-region mechanics through the nonlinear conservation laws and the constitutive equations. The latter ought ultimately to be based upon laboratory experiments, inference from field experiment, micromechanical modeling, or all of these.

We can, of course, achieve at least a minimal understanding of the seismic source without actually modeling the nonlinear deformation. The cumulative effect of source-region deformation is to exert a radial stress on the spherical surface at the elastic radius r_e . As a first approximation one can neglect the time dependence of this stress pulse and treat the problem in which its static level is applied instantaneously. This is the classic cavity source problem, whose well-known solution is

$$\hat{\psi}(w) = \frac{\hat{P}_c(w) r_e^3}{4\rho\beta^2} \frac{e^{-iw(r-r_e)/\alpha}}{1 - i \frac{r_e}{\alpha} w - \frac{r_e^2}{4\beta^2} w^2} \quad (A.1)$$

where $P_c(t)$ is the pressure applied to the interior cavity wall, starting from a quiescent state at time $t = 0$. The exterior wholespace is isotropic, homogeneous, linearly elastic. The exterior wavespeeds and densities are denoted by α , β and ρ .

This source spectrum when $P_c(t)$ is approximated by a step $P_0 H(t)$ is only slightly peaked near the corner frequency, and the corresponding far-field waveform has very little overshoot.

For the most part, dynamic treatment of nonlinear deformation within the source region requires numerical solutions to the governing partial differential equations. However, it is very useful to have available analytical results which

aid in the interpretation of numerical solutions. In particular, it would be useful to have some insight into the dynamic behavior engendered by a weakened shell of rock near the explosion cavity, abutted by stronger rock. This is the sort of strength contrast we would expect to develop dynamically under strain-weakening or shock-conditioning conditions, for example.

For the purpose of developing analytical solutions, these circumstances can only be represented in a very rough manner. By analyzing two very different idealizations, however, we will have developed some interpretive tools with which to appreciate more rigorous numerical simulations.

In this appendix, we first investigate weakening effects through a simple extension of the linear cavity source problem. Then, nonlinear effects, both geometrical and material, will be introduced in a simplified manner.

Neglecting gravity and assuming linear elasticity pertains, we consider a spherical bubble of radius r_1 in the center of a fluid-filled cavity of radius r_2 in an elastic wholespace (Figure A.1). The interior and exterior wavespeeds and densities are denoted by subscripts 1 and 2, respectively.

The bubble is pressurized with a given pressure time history $P_C(t)$. The solution for the displacement s then has the frequency-domain form

$$\hat{s} = - \frac{\partial \hat{\phi}}{\partial r} \quad (A.2)$$

where

$$\hat{\phi} = \begin{cases} \hat{A} \frac{e^{-i\omega r} \alpha}{r} - \hat{B} \frac{e^{i\omega r} \alpha}{r} & \text{in fluid,} \\ \hat{C} \frac{e^{-i\omega r} \alpha}{r} & \text{in solid.} \end{cases} \quad (A.3)$$

a_1 = Fluid sound speed

ρ_1 = Fluid density

a_2 = Exterior P wavespeed

β_2 = Exterior S wavespeed

ρ_2 = Exterior density

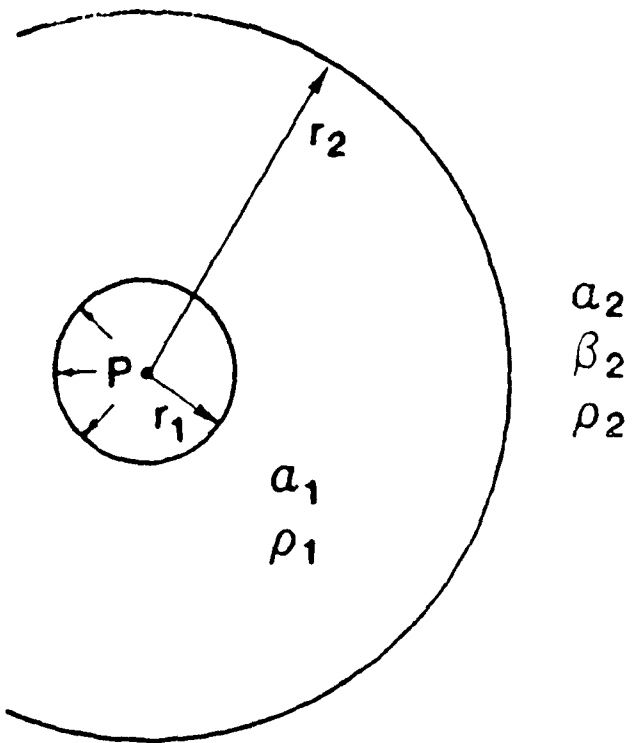


Figure A 1. Problem geometry for fluid-filled cavity-source.

the coefficients \hat{A} , \hat{B} and \hat{C} to be determined from the boundary and continuity conditions

$$\hat{T}_{rr}(r_1) = -\hat{P}_C \quad (A.4)$$

$$\hat{T}_{rr} \text{ continuous at } r_2 \quad (A.5)$$

$$\hat{s} \text{ continuous at } r_2 \quad (A.6)$$

The radial stress in terms of ϕ is

$$\begin{aligned} \hat{T}_{rr} &= (\lambda - 2\mu) \frac{\partial s}{\partial r} - 2\lambda \frac{\hat{s}}{r} \\ &= - \left[(\lambda - 2\mu) \frac{\partial^2 \phi}{\partial r^2} \right] - \frac{2\lambda}{r} \frac{\partial \phi}{\partial r} \end{aligned} \quad (A.7)$$

The three boundary/continuity conditions become

$$-\hat{P}_C = \rho_1 \frac{\omega^2}{r_1^2} \left[\hat{A} e^{-i\omega r_1/\alpha_1} - \hat{B} e^{i\omega r_1/\alpha_1} \right] \quad (A.8)$$

$$\rho_1 \frac{\omega^2}{r_2^2} \left[\hat{A} e^{-i\omega r_2/\alpha_1} - \hat{B} e^{i\omega r_2/\alpha_1} \right] = - \frac{4\rho_2 \beta_2^2}{r_2^3} C \hat{C} e^{-i\omega r_2/\alpha_2} \quad (A.9)$$

$$\begin{aligned} \left(\frac{1}{r_2^2} - \frac{i\omega}{\alpha_1 r_2} \right) \hat{A} e^{-i\omega r_2/\alpha_1} - \left(\frac{1}{r_2^2} + \frac{i\omega}{\alpha_1 r_2} \right) \hat{B} e^{i\omega r_2/\alpha_1} \\ = \left(\frac{1}{r_2^2} + \frac{i\omega}{\alpha_2 r_2} \right) \hat{C} e^{-i\omega r_2/\alpha_2} \end{aligned} \quad (A.10)$$

where

$$q = 1 - i \frac{r_2}{a_2} \omega - \frac{r_2^2}{4\beta_2^2} \omega^2 \quad (A.11)$$

Solve Equation (A.10) for $\hat{C} e^{-i\omega r_2/a_2}$ and substitute into Equation (A.9). This turns Equations (A.8) and (A.9) into the system for \hat{A} and \hat{B} :

$$a_1 \hat{A} - b_1 \hat{B} = -\hat{P}_c \quad (A.12)$$

$$a_2 \hat{A} - b_2 \hat{B} = 0 \quad (A.13)$$

In Equations (A.12) and (A.13), the coefficients are

$$a_1 = \rho_1 \frac{\omega^2}{r_1} e^{-i\omega r_1/a_1} \quad (A.14)$$

$$b_1 = \rho_1 \frac{\omega^2}{r_1} e^{-i\omega r_1/a_1} \quad (A.15)$$

$$a_2 = \left[\rho_1 \frac{\omega^2}{r_2} - \frac{4\rho_2 \beta_2^2}{r_2^3} q \left(\frac{1}{r_2^2} - \frac{i\omega}{a_2 r_2} \right)^{-1} \left(\frac{1}{r_2^2} - \frac{i\omega}{a_1 r_2} \right) \right] e^{-i\omega r_2/a_1}$$

$$b_2 = \left[\rho_1 \frac{\omega^2}{r_2} - \frac{4\rho_2 \beta_2^2}{r_2^3} q \left(\frac{1}{r_2^2} - \frac{i\omega}{a_2 r_2} \right)^{-1} \left(\frac{1}{r_2^2} - \frac{i\omega}{a_1 r_2} \right) \right] e^{-i\omega r_2/a_1} \quad (A.17)$$

The Cramer's rule solution for \hat{A} and \hat{B} is

$$\hat{A} = \frac{-b_2 \hat{P}_c}{a_1 b_2 - a_2 b_1} \quad , \quad (A.18)$$

$$\hat{B} = \frac{a_2 \hat{P}_c}{a_1 b_2 - a_2 b_1} \quad , \quad (A.19)$$

which we plug into Equation (A.10) and solve for \hat{C} . The expression then simplifies to

$$\hat{C} = \frac{\hat{P}_c r_1 r_2^2}{4 \rho_2 \beta_2^2} \frac{e^{-i\omega(r-r_2)/a_2}}{q (\cos \theta - a \sin \theta)} \quad , \quad (A.20)$$

where

$$q = 1 - i \frac{r_2}{a_2} \omega - \frac{r_2^2 \omega^2}{4 \rho_2^2} \quad , \quad (A.21)$$

$$\theta = \frac{\omega (r_2 - r_1)}{a_1} \quad , \quad (A.22)$$

$$a = \frac{\rho_1 \omega a_1 r_2}{4 \rho_2 \beta_2^2 q} \left(1 - \frac{i \omega r_2}{a_2} \right) - \frac{a_1}{r_2 \omega} \quad , \quad (A.23)$$

Equation (A.20) gives the reduced displacement potential, which we have heretofore called \hat{s} . Thus, \hat{s} is given by

$$\hat{s} = \left[\frac{1}{r^2} - \frac{i\omega}{a_2 r} \right] \frac{\hat{P}_C r_1 r_2^2}{4\rho_2 \beta_2^2} \frac{e^{-i\omega(r-r_2)/a_2}}{q (\cos \theta - a \sin \theta)} \quad (A.24)$$

In the high-frequency limit, Equation (A.24) has a nice interpretation. We can rewrite it as

$$\hat{s}(r, \omega) = \frac{\hat{P}_C r_1 r_2^2}{4\rho_2 \beta_2^2 q} \frac{2e^{-i\theta}}{(1-ia)} \frac{e^{-i\omega(r-r_2)/a_2}}{\left[1 - e^{-2i\theta} \left(\frac{ia-1}{ia+1} \right) \right]} \left(\frac{1}{r^2} - \frac{i\omega}{r a_2} \right) \quad (A.25)$$

The high-frequency limit of Equation (A.25), for the case of P_C equal to a step function of amplitude P_0 is

$$\hat{s}(r, \omega) \sim e^{-i\omega(r-r_2)/a_2} \frac{(-P_0) r_1}{\rho_1 a_1 r \omega^2} T e^{-i\theta} (1 \cdot R e^{-2i\theta} - R^2 e^{-4i\theta} \dots) \quad (A.26)$$

where

$$R = \frac{\rho_2 a_2 + \rho_1 a_1}{\rho_2 a_2 - \rho_1 a_1} \quad (A.27)$$

$$T = \frac{2\rho_1 a_1}{\rho_2 a_2 - \rho_1 a_1} \quad (A.28)$$

$$\theta = \frac{\omega(r_2 - r_1)}{a_1} \quad (A.29)$$

Equations (A.27), (A.28) and (A.29), respectively, are the normal incidence plane wave reflection coefficient (R) and transmission coefficient (T) at the fluid-solid boundary, and the one-way phase delay (θ) across the fluid shell. Thus, Equation (A.26) has an obvious interpretation. At sufficiently high frequency, the radius of curvature of all boundaries eventually becomes negligible compared with the wavelength. The series terms then represent multiple reflections at the fluid-solid interface. The first motion of each reflection is given by the inverse transform of the corresponding series term (Abel's theorem) giving the following first motion series, most easily expressed in terms of velocity:

$$u(r, t) \sim \frac{P_0 r_1}{\rho_1 a_1 r} T \sum_{n=0}^{\infty} (-)^n R^n H \left[t - \frac{r-r_2}{a_2} - \frac{2n(r_2-r)}{a_1} \right] \quad (A.30)$$

where H is the unit step function.

Thus, the fluid shell gives rise to repeated overshoot and rebound in the motion, as well as the potential, at r_2 . This tends to put a stronger peak into the far-field displacement spectrum. In a real material, there would be some residual strength after strain-weakening (or shock conditioning, or whatever weakening mechanism is postulated to operate), and this would rapidly damp the oscillation of the source region, probably after a single cycle of outward motion and rebound. Nonlinear numerical simulations with shock weakening (effective stress law, for example) indeed exhibit this enhanced rebound and spectral peaking.

Figure A.2 shows some complete time histories for the reduced displacement potential for the fluid-shell problem, in which the overshoot and rebound are evident. The extent of overshoot seems to increase with the extent of the fluid shell region.

The preceding solution to the linearized momentum equation with elastic stress-strain relation is useful in its own right, in that it demonstrates that strain weakening near the source, represented here as an approximate way by introducing a fluid, (zero-strength) interior shell, can lead to reverberative response. As noted above, it seems likely that if the interior region were a soft, plastic shell instead of a fluid, one might still see the outgoing pulse (first term in

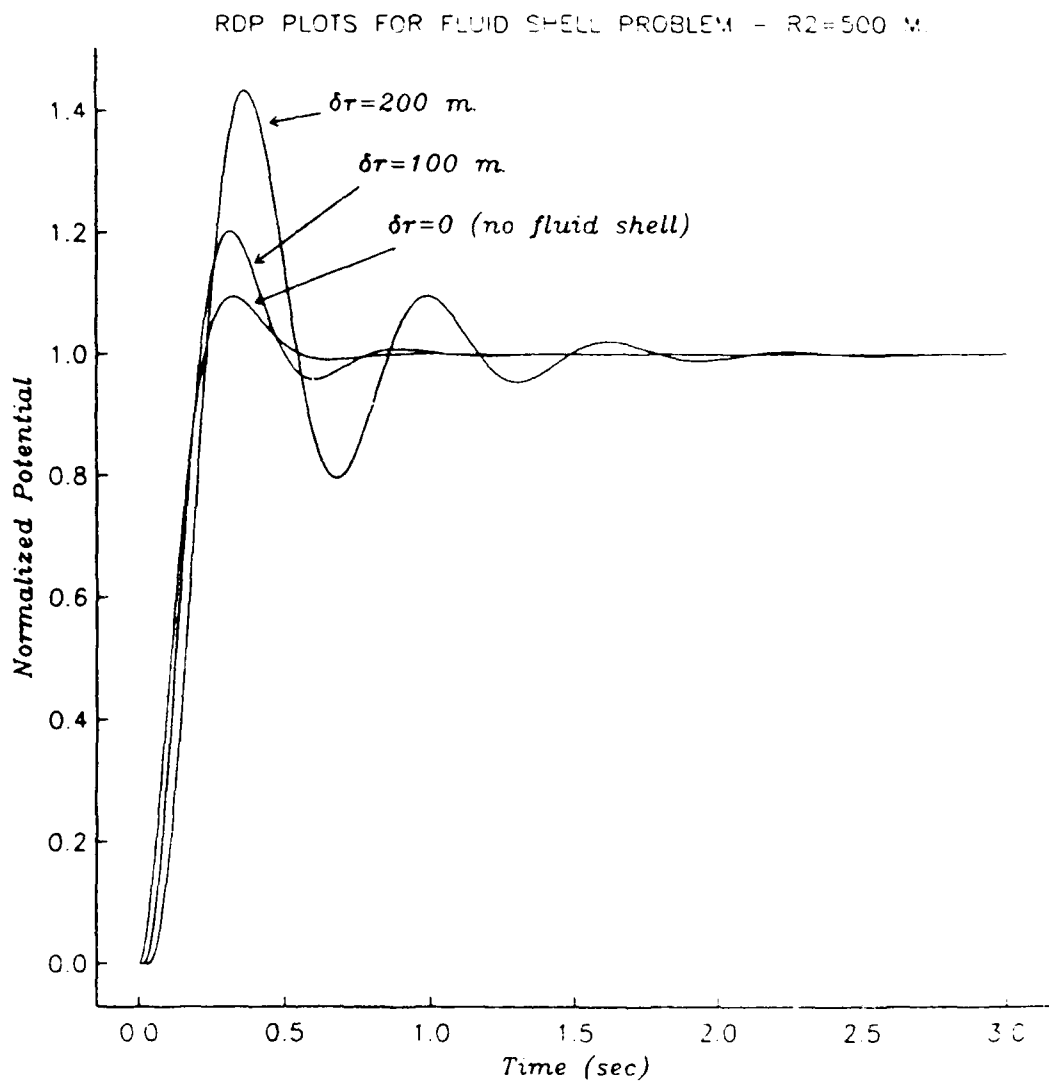


Figure A.2. Some numerical solutions to the fluid shell problem. The shell thickness $r_2 - r_1$ is denoted by δr . Density is 2500 kg m^{-3} everywhere. P wavespeed is 5000 m sec everywhere, and the exterior shear wavespeed is 3000 m sec , and the fluid bulk Q is 10.

Equation A 30) with somewhat diminished amplitude, the first rebound (second term in Equation A.30), also diminished in amplitude, and then locking in of the cavity displacement due to the strength of the plastic shell. This would be analogous to the oscillation followed by locking of a harmonic oscillator to which a Coulomb slider has been added. If this qualitative description is correct, then strain weakening should lead to a source function with significant overshoot. To make this notion more quantitative, we seek the help of an analytic solution. This calculation is a useful supplement to the last section, as it incorporates both geometrical and material nonlinearity. The price paid is that the source region is treated as incompressible, which leads to unphysical behavior of the first motion. Furthermore, we manage only to reduce the problem to that of solving a system of three coupled first-order ordinary differential equations. These are easily solved numerically, however.

Figure A.3 shows a spherical shell of interior radius $r_1(t)$ and exterior radius $r_2(t)$, both of which are time varying. The left hand side is the initial configuration, at $t = 0$, the right hand side is the configuration at some later time t . The shell consists of a rigid-perfectly plastic, incompressible solid in welded contact with a linearly elastic wholespace at r_2 . The shell has density ρ_1 and yield strength Y ; the wholespace has density, P wavespeed and S wavespeed equal to ρ_2 , a_2 and β_2 , respectively.

We wish to find the seismic radiation when the shell is loaded at time zero by a pressure P_C , which may in turn depend nonlinearly upon the motion.

The radial coordinate in the initial, undeformed configuration will be our reference, or Lagrangian, coordinate, denoted R . The corresponding spatial coordinate will be denoted $r = r(R,t)$, so that $r(R,0) = R$.

From the incompressibility condition, we have

$$\rho(R,t) = \rho(R,0) \text{ for } R_1 < R < R_2 \quad (\text{A } 31)$$

and the continuity equation under spherical symmetry, combined with Equation (A 31), gives

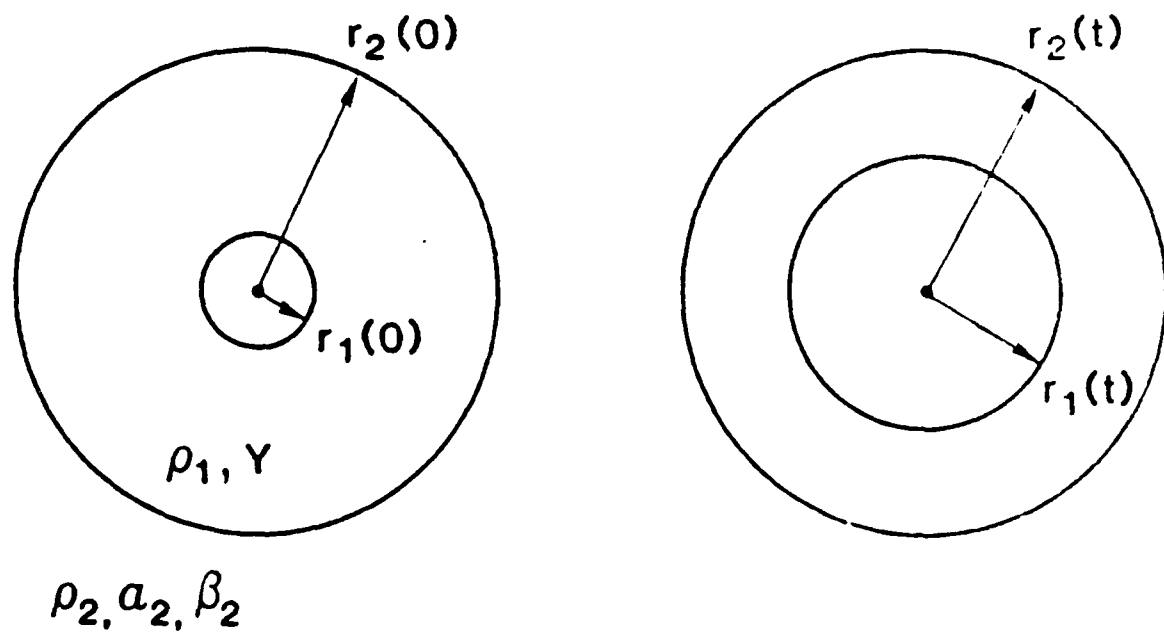


Figure A 3 Problem geometry for the plastic-filled cavity source

$$\frac{r^2}{R^2} \frac{\partial r}{\partial R} = \text{constant for } R_1 < R < R_2 \quad (A.32)$$

Integrating Equation (A.32) we get

$$r(R, t) = \left[R^3 - r^3 (R_0, t) - R_0^3 \right]^{1/2} \quad R_1 < R < R_2 \quad (A.33)$$

where R_0 is some reference position. The radial displacement s is then

$$\begin{aligned} s(R, t) &= \left[R^3 - r^3 (R_0, t) - R_0^3 \right]^{1/3} - R \\ &= \left[R^3 - s_0 \left[s_0^2 - 3R_0 s_0 - 3R_0^3 \right] \right]^{1/3} - R \end{aligned} \quad (A.34)$$

(From now on we will drop the argument t when there is no ambiguity.) Some limits:

$$\text{for } s_0 \ll R_0 \quad s(R) \sim s_0 \left(\frac{R_0}{R} \right)^2 \quad (A.35)$$

$$\text{for } s_0 \gg R \quad s(R) \sim s_0 - R_0 - R \quad (A.36)$$

Next we deal with the momentum conservation equation under spherical symmetry

$$\rho \frac{du}{dt} = \frac{\partial T_{rr}}{\partial r} - \frac{2}{r} (T_{rr} + T_{\theta\theta}) \quad (A.37)$$

The plastic yield condition is

$$|T_{rr} - T_{\theta\theta}| \leq Y. \quad (A 38)$$

Because of the rigid-plastic, incompressible conditions there can be no motion unless the whole plastic shell is at the yield surface, then

$$\rho \frac{d^2 s}{dt^2} = \frac{\partial T_{rr}}{\partial r} - \frac{2}{r} \operatorname{sgn}(u) Y. \quad (A 39)$$

the solution to which we seek, with the boundary conditions

$$T_{rr}(r_1) = -P \quad (A 40)$$

$$T_{rr}(r_2) = T_2. \quad (A.41)$$

The outer boundary stress T_2 is to be determined by requiring continuity between the interior plastic solution and the exterior elastic solution, which is just the cavity source problem with $P_c = -T_2$. Substituting $P_c = -T_2$ into Equation (A.1), and making the operational interpretation $\omega = d/dt$, leads to the following ordinary differential equation for $s_2 = s(r_2, t)$:

$$s_2 - \frac{r_2}{a_2} s_2 - \left(\frac{r_2}{2\beta_2} \right)^2 s_2 = \frac{-r_2}{4\rho_2 \beta_2^2} \left(T_2 - \frac{r_2}{a_2} T_2 \right). \quad (A 42)$$

If we can express the solution to Equation (A.39) in terms of the unknown boundary value T_2 , then that expression, combined with Equation (A.42), will constitute an ordinary differential equation system which we can solve for s_2 and T_2 . Then the source function ψ in terms of s_2 is given by the convolution

$$\psi(t) = a_2 r_2 e^{-a_2 t} r_2 * s_2(t). \quad (A 43)$$

To solve Equation (A.39), we integrate with respect to r :

$$T_{rr}(r) = -P_c - 2Y \operatorname{sgn}(u) \ln \frac{r}{r_1} - \rho \int_{r_1}^r u(r') dr \quad (A.44)$$

Next, evaluate the final term in Equation (A.44) in terms of s_2 . The velocity is

$$u(r, t) = \frac{\partial s}{\partial t} \Big|_{R=R(r)} \quad (A.45)$$

where $R(r)$ is the inverse function of $r(R)$. From Equation (A.34), we get

$$u(r, t) = s_2 \left(\frac{r_2}{r} \right)^2 \quad (A.46)$$

The acceleration is

$$\begin{aligned} \frac{d^2 s}{dt^2} &= \frac{du}{dt} = \frac{\partial u}{\partial t} \Big|_{R} = \frac{\partial u}{\partial t} \Big|_r - u \frac{\partial u}{\partial r} \Big|_t \\ &= s_2 \left(\frac{r_2}{r} \right)^2 - 2 s_2^2 \frac{r_2}{r^2} \left(1 - \frac{r_2^3}{r^3} \right) \end{aligned} \quad (A.47)$$

Plugging Equation (A.47) into Equation (A.44) and carrying out the integration leads to an expression for $T_{rr}(r, t)$, which we evaluate at $r = r_2$:

$$T_2(t) = -P_c - 2Y \operatorname{sgn}(s_2) \ln \frac{r_2}{r_1} - \rho_1 \frac{r_2}{r_1} \delta r \left(s_2 - \frac{2}{r_2} s_2^2 \right)$$

$$- \rho_1 \frac{\left[r_2^4 - r_1^4 \right]}{2 r_1^4} s_2^2 \quad . \quad (A.48)$$

$$\text{where } \delta r \equiv r_2 - r_1$$

We could substitute Equation (A.48) into Equation (A.42) to obtain a third-order ordinary differential equation for $s_2(t)$. This equation is completed by specifying $P_c(r_1)$ via an equation of state, e.g., the constant-gamma gas approximation

$$P_c = \frac{3(\gamma-1)W}{4\pi R_1^3} \left(\frac{R_1}{r_1} \right)^{3\gamma} \quad . \quad (A.49)$$

where W is the explosion energy. Equation (A.48) is nonlinear in s_2 , and therefore Equation (A.42) generally will require a numerical method for its solution.

A more convenient form for numerical treatment ensues if we define the new dependent variable τ ,

$$\tau \equiv s_2 - \frac{T_2}{\rho_2 a_2} \quad . \quad (A.50)$$

Then we define the vector components V_i by

$$V_1 \equiv \tau \quad (A.51a)$$

$$V_2 \equiv s_2 \quad (A.51b)$$

$$V_3 \equiv s_2 \quad (A.51c)$$

With these definitions, Equations (A.42) and (A.48) are equivalent to the following system of first order ordinary differential equations:

$$\frac{dV}{dt} = F(V, t) \quad . \quad (A.52)$$

where

$$F_1 = - \frac{4\beta_2^2}{r_2^2} \left[V_3 - \frac{r_2}{a_2} \left(1 - \frac{a_2^2}{4\beta_2^2} \right) V_2 \right] - \frac{a_2}{r_2} V_1 \quad . \quad (A.53a)$$

$$F_2 = \frac{r_1 a_2 \rho_2}{r_2 \delta r \rho} \left\{ V_1 - \frac{P_c(r_1)}{\rho_2 a_2} - V_2 \cdot \frac{2 Y \operatorname{sign}(V_2)}{\rho_2 a_2} \ln \frac{r_2}{r_1} \right. \quad .$$

$$\left. - \frac{2\rho_1}{a_2 \rho_2 r_1} \left[\delta r - \frac{(r_2^4 - r_1^4)}{4 r_1^3} \right] V_2^2 \right\} \quad . \quad (A.53b)$$

$$F_3 = V_2 \quad . \quad (A.53c)$$

Recall that r_1 is a known function of s_2 , given by Equation (A.34) (by virtue of the incompressibility condition), and that $P_c(r_1)$ is given by Equation (A.49). Equation (A.52) is easily solved using a fourth-order Runge-Kutta method, with due caution regarding the sign of V_2 in the fourth term of Equation (A.53b).

Because of the incompressibility condition, Equation (A.52) is unphysical in its representation of the first motion, and probably generally smooths out high-frequency features which would appear if compressibility were permitted. This smoothing is evident in numerical results shown in Figure A.4. In all cases shown, the explosion energy is 50 KT, emplaced in a cavity of initial radius 10 m.

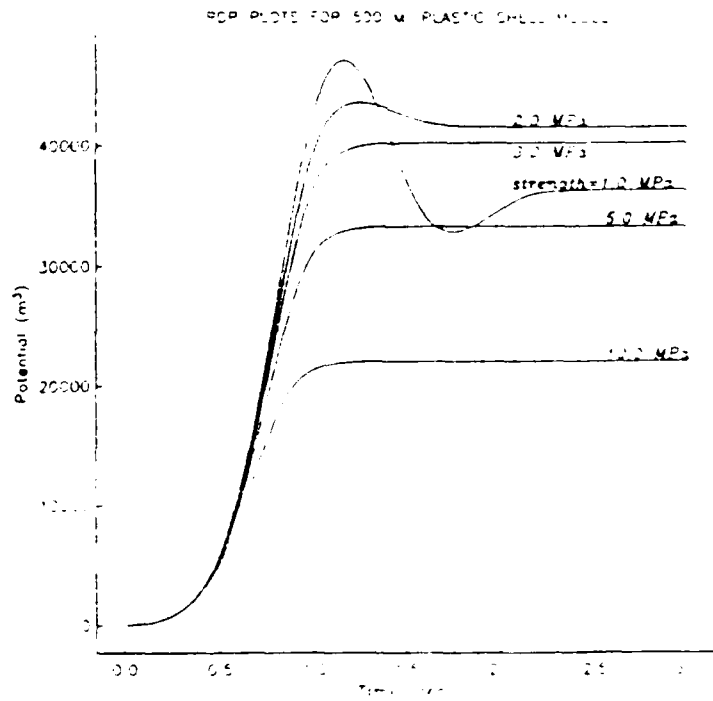
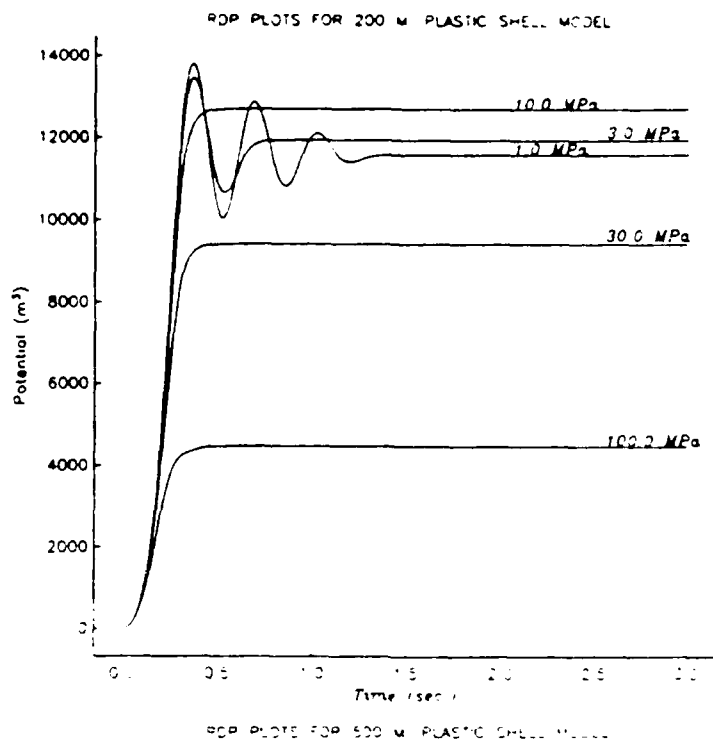


Figure A 4 Some numerical solutions to the plastic shell problem

density and exterior wavespeeds are, respectively, 2500 kg/m^3 , 5000 m/sec , and 3000 m/sec . Results are given in terms of the reduced displacement potential, via Equation (A.43). The first motion is quadratic in time rather than linear, an artifact of the incompressibility condition. When the shell is weak, the anticipated overshoot appears, and damps out rapidly, as expected. When the shell is weak enough that several half-cycles appear, the oscillation amplitude diminishes by an approximately constant decrement at each half cycle. This behavior roughly mimics that of a harmonic oscillator in parallel with a Coulomb slider. Thus, in spite of some severe oversimplification, this solution verifies that shock conditioning is responsible for introducing or enhancing overshoot in the source function.

APPENDIX B

STRAIN PATHS, TIME HISTORIES AND REDUCED DISPLACEMENT POTENTIALS FOR GRANITE CALCULATIONS

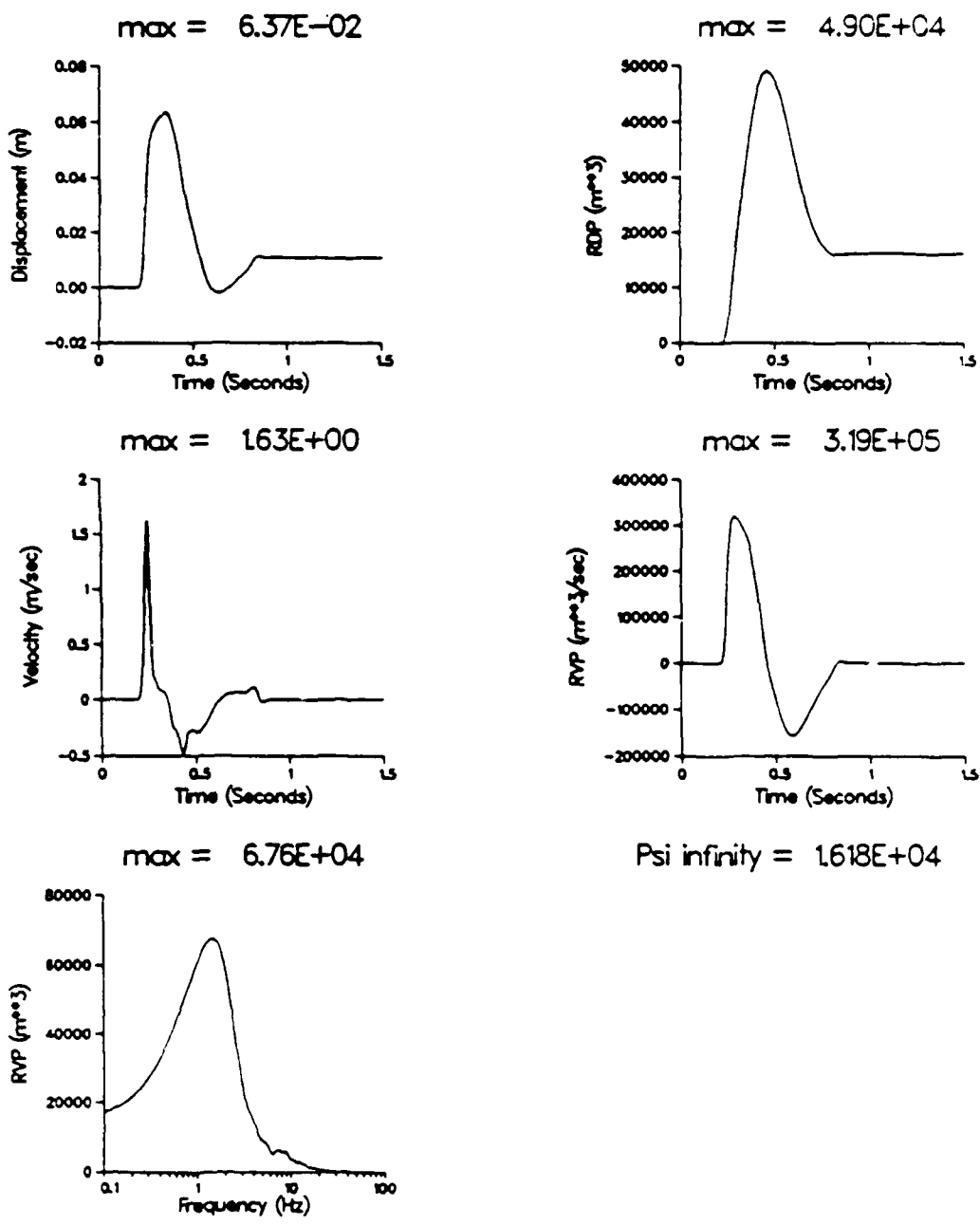


Figure B.1. Reduced displacement potential, reduced velocity potential, and displacement and velocity at 1225 meters for PILEDRIVER Calculation Number 570.

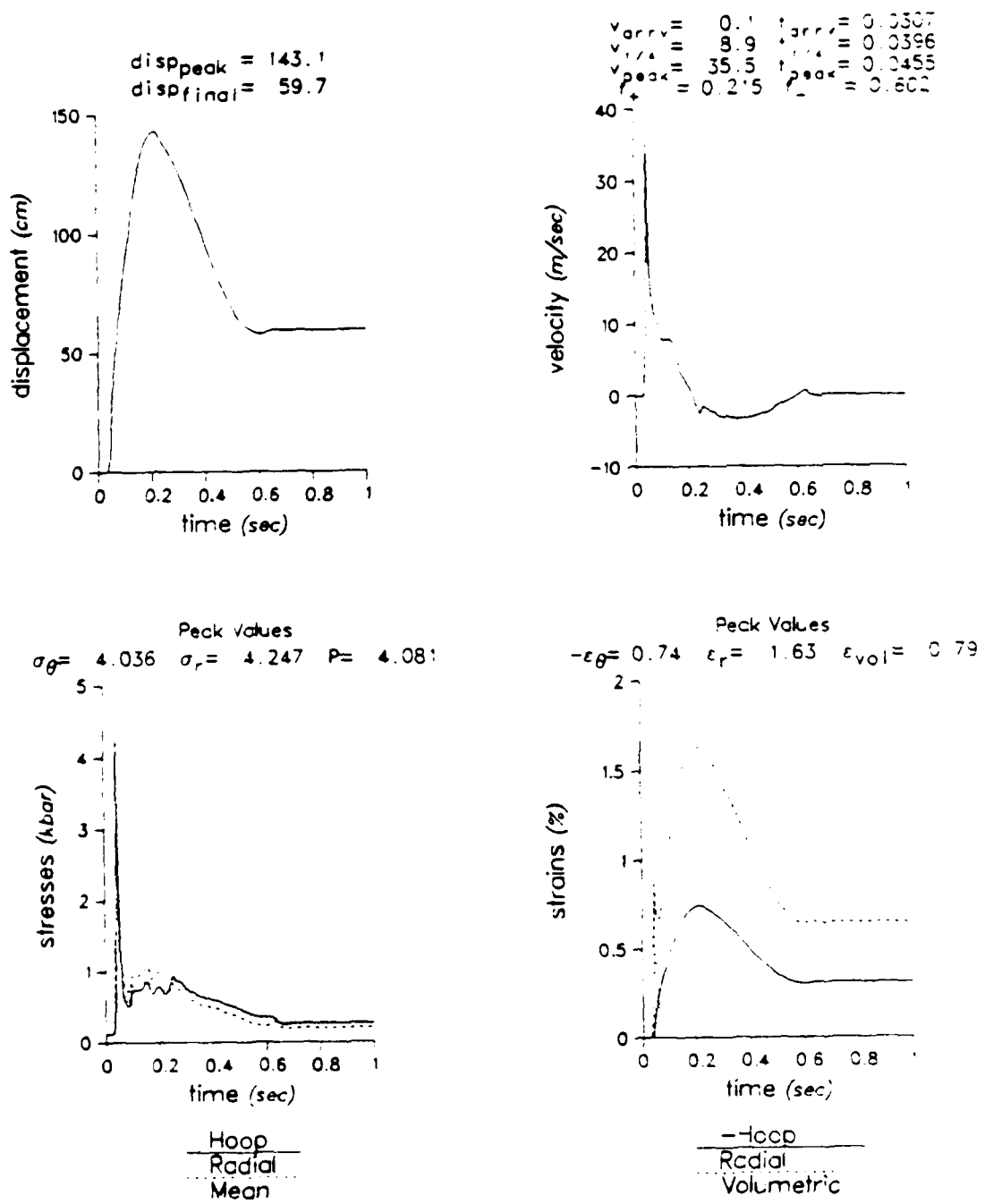


Figure B.2 Displacement, velocity, stress and strain time histories at 204 meters for PILEDRIVER Calculation Number 570

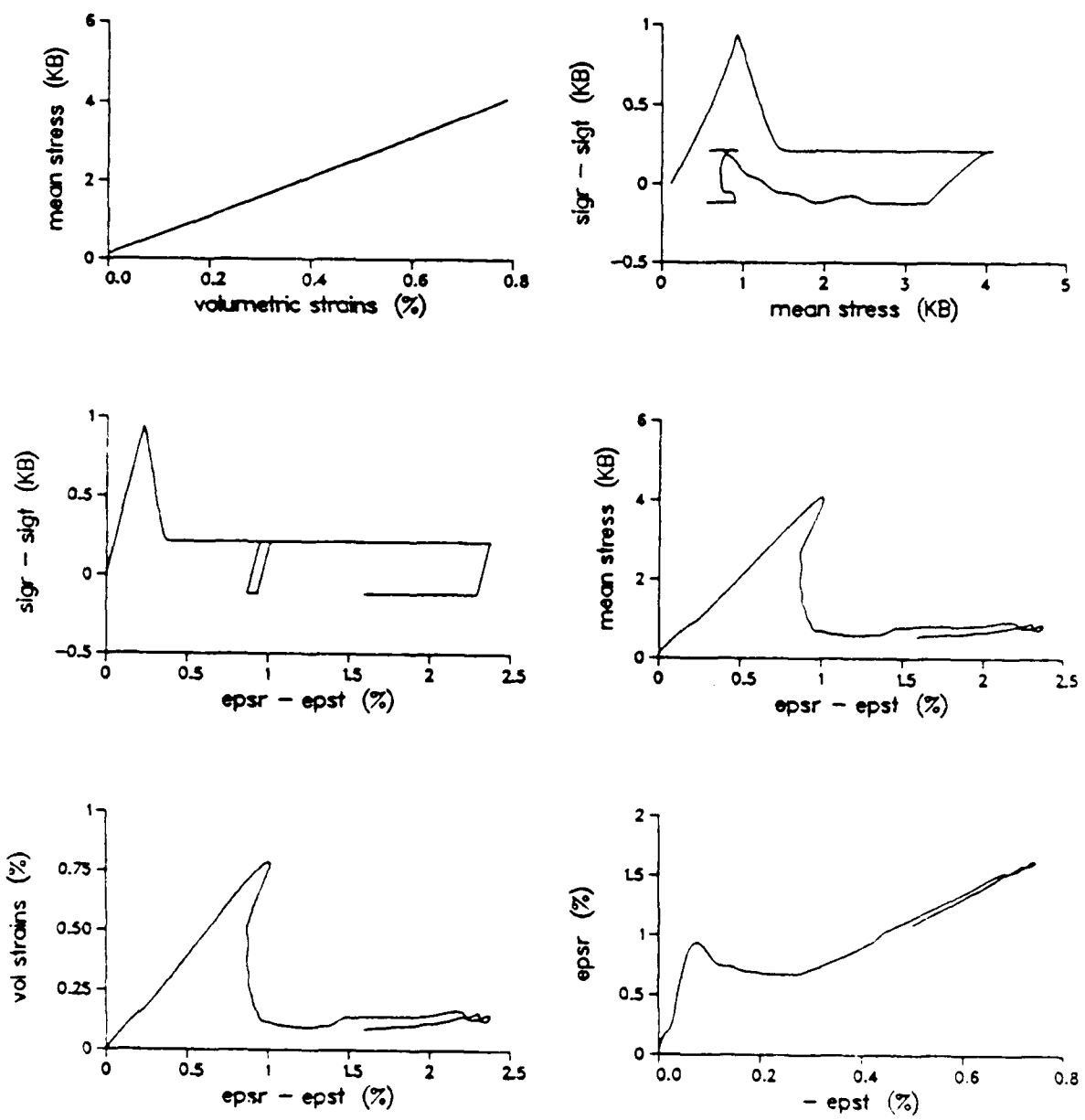


Figure B.3. Strain paths at 204 meters for PILEDRIVER Calculation Number 570.

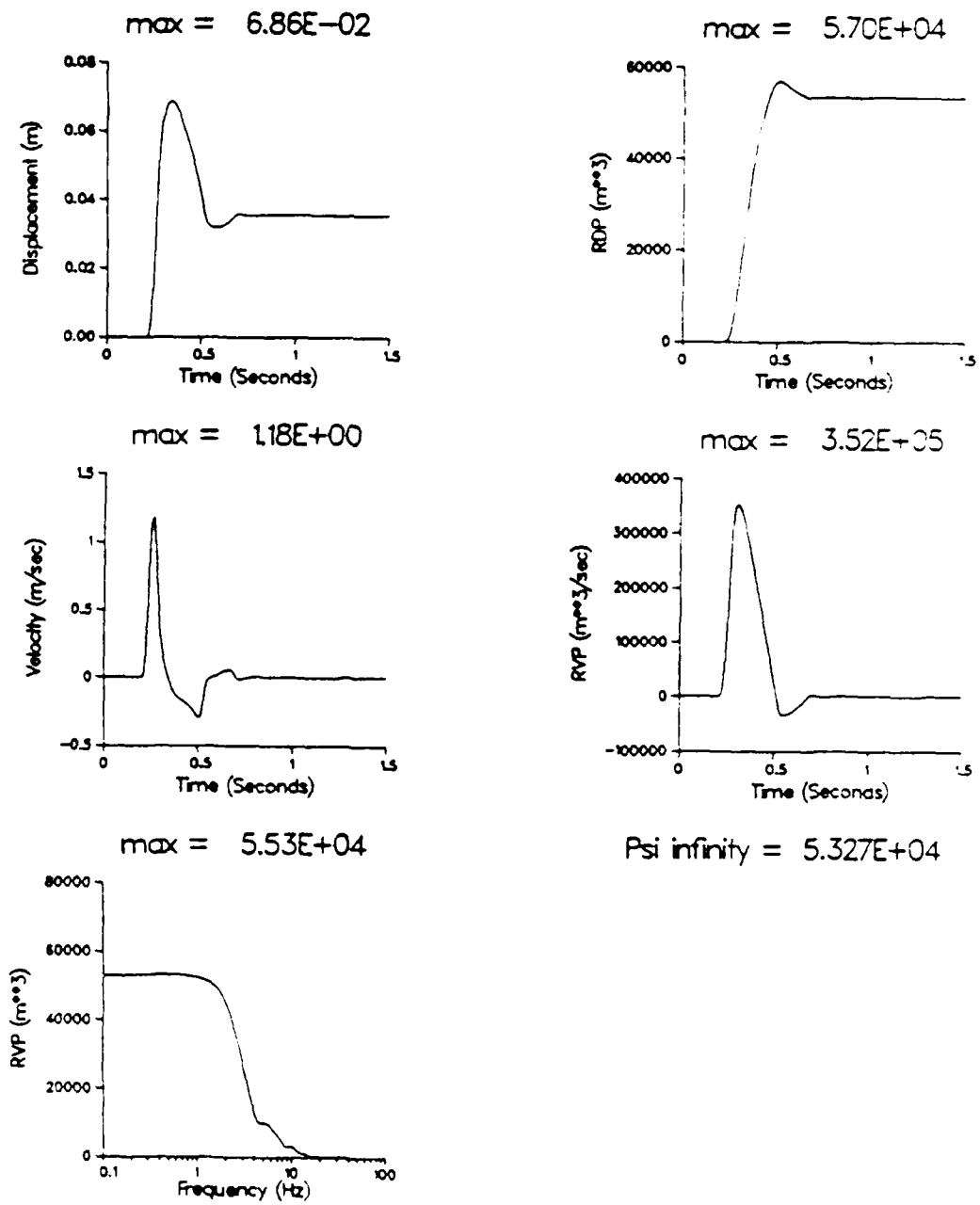


Figure B.4 Reduced displacement potential, reduced velocity potential, and displacement and velocity at 1225 meters for weak calculation (strength = 200 bars).

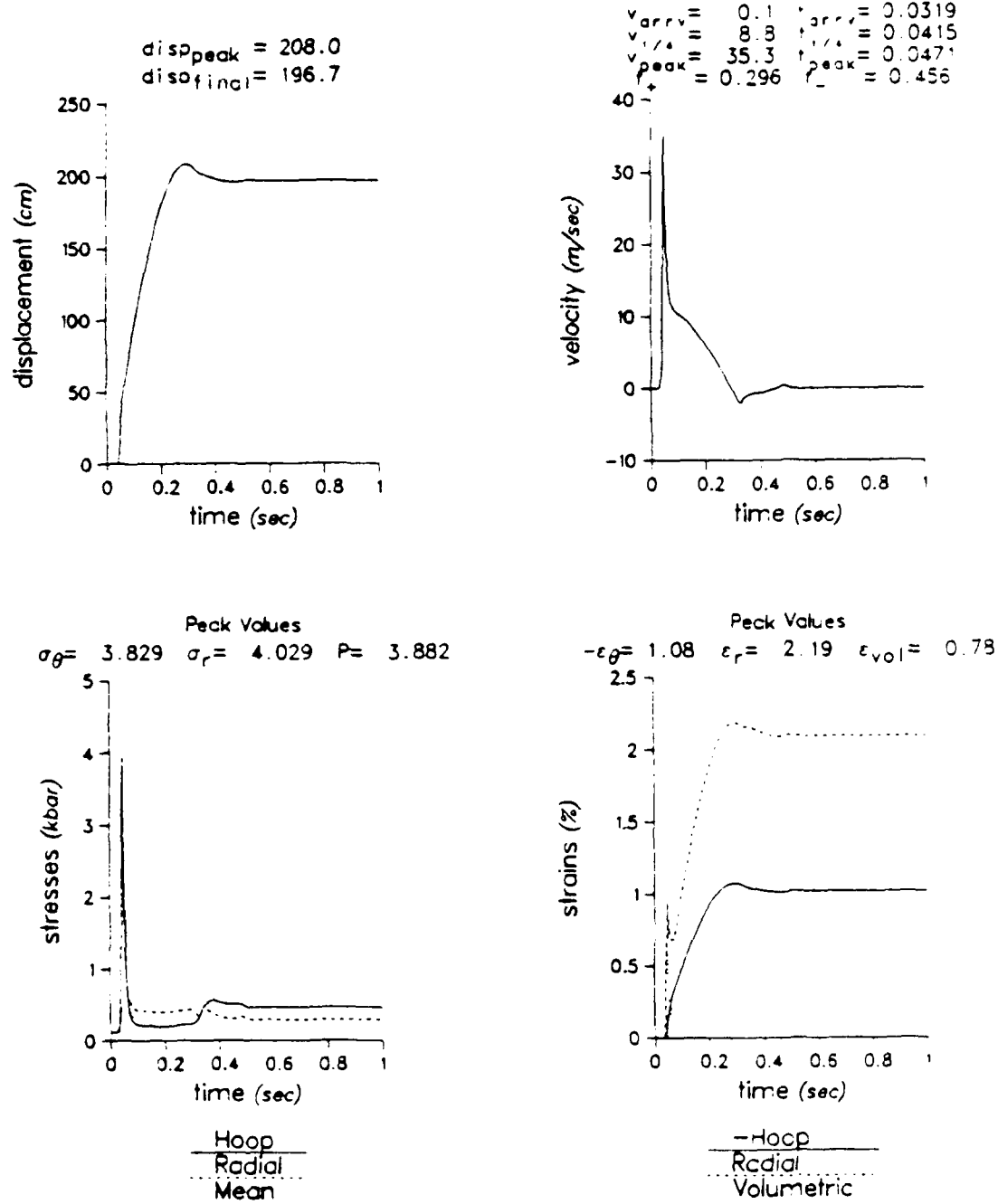


Figure B 5. Displacement, velocity, stress and strain time histories at 204 meters for weak calculation (strength = 200 bars)

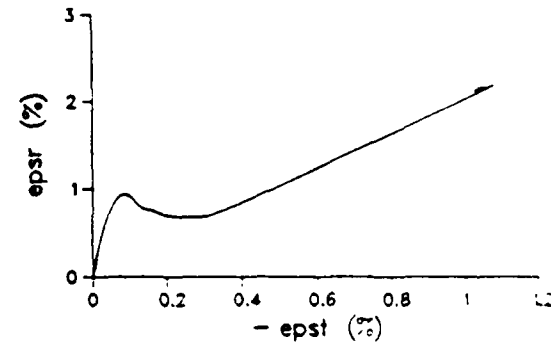
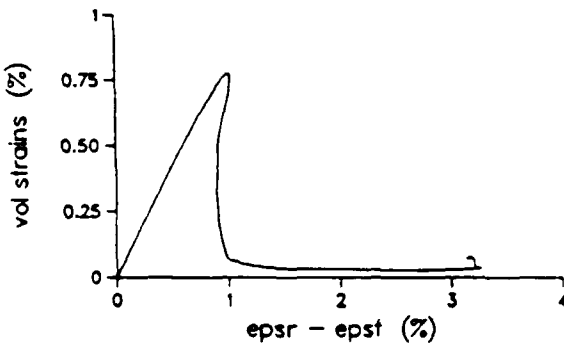
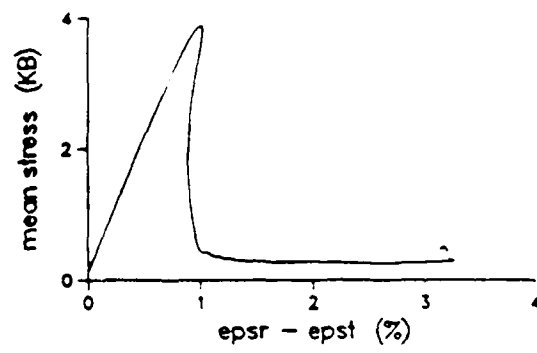
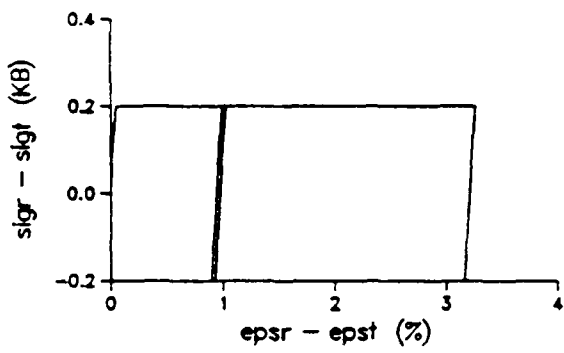
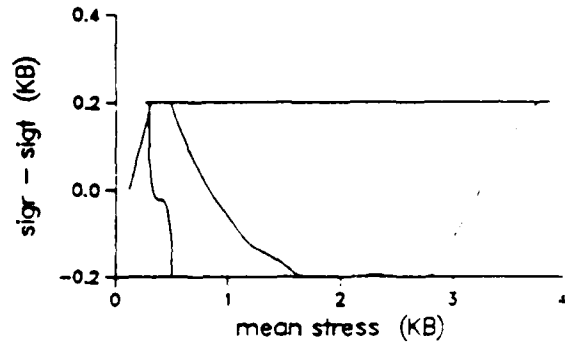
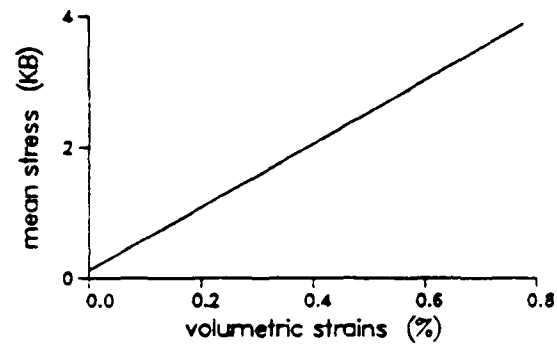


Figure B 6 Strain paths at 204 meters for weak calculation (strength = 200 bars).

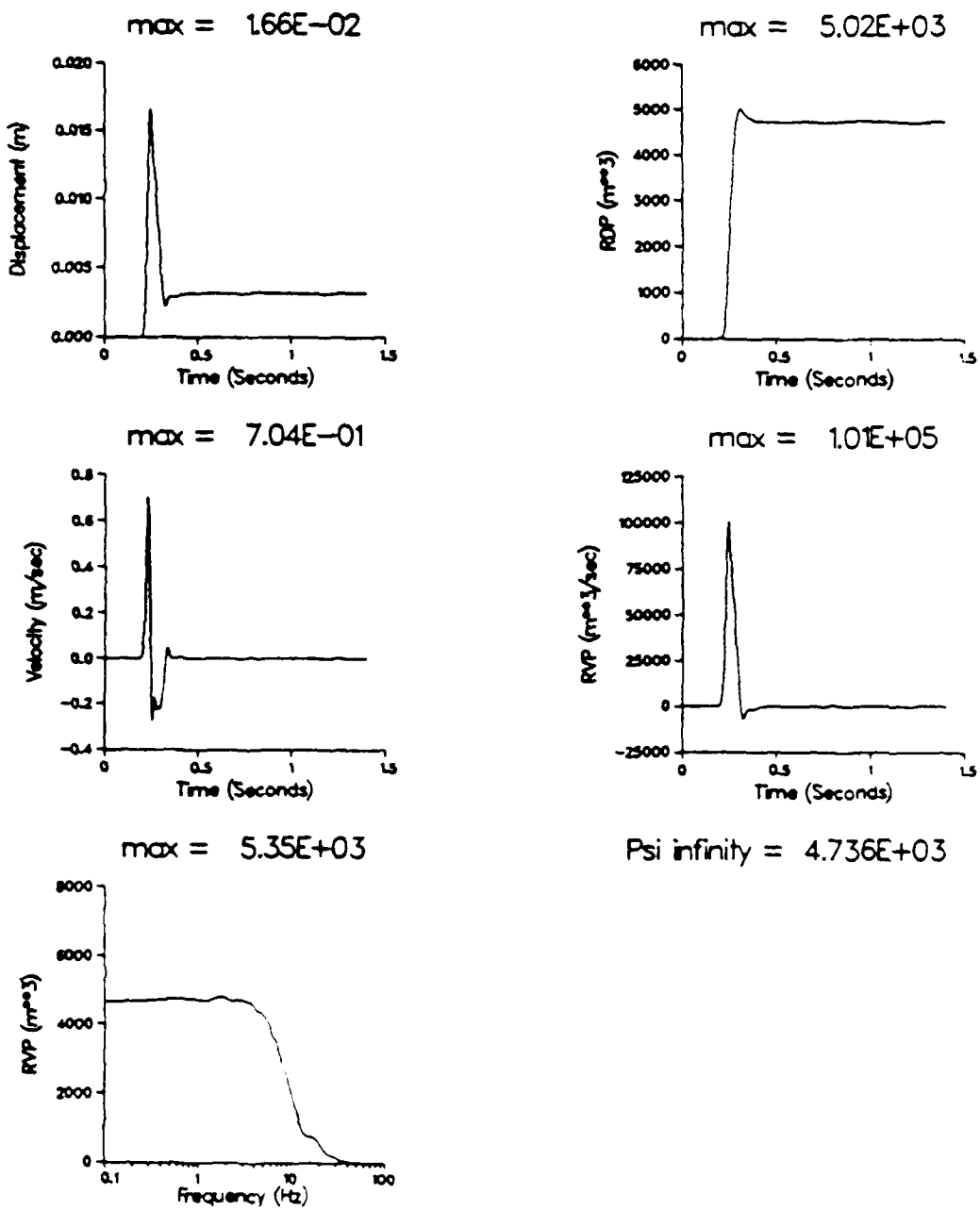


Figure B.7. Reduced displacement potential, reduced velocity potential, and displacement and velocity at 1225 meters for high laboratory strength calculation - radial return flow rule

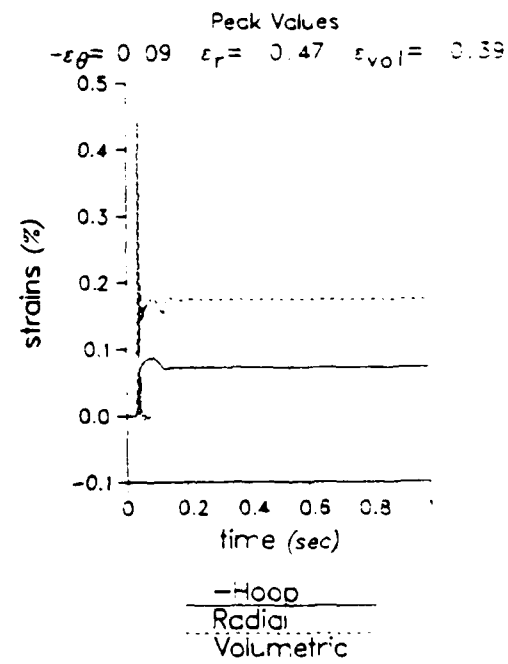
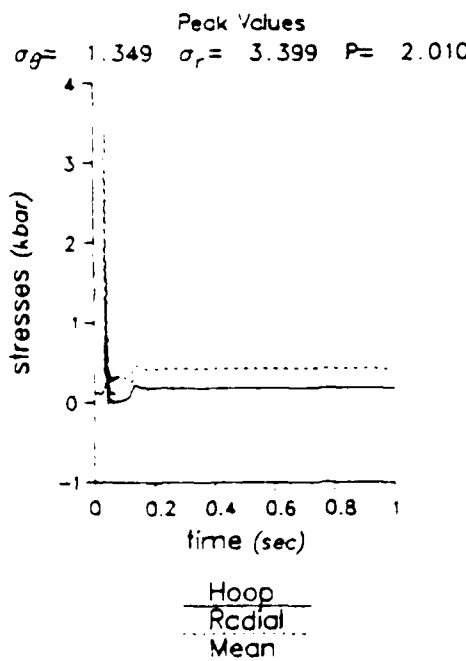
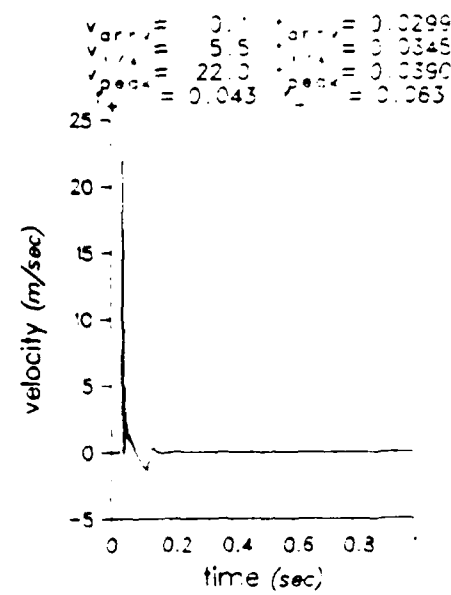
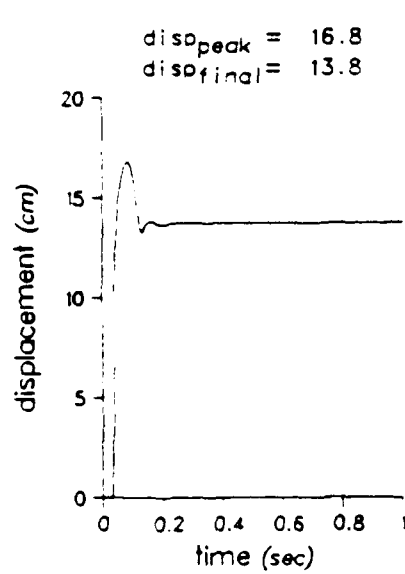


Figure B 8 Displacement, velocity, stress and strain time histories at 204 meters for high laboratory strength calculation - radial return flow rule.

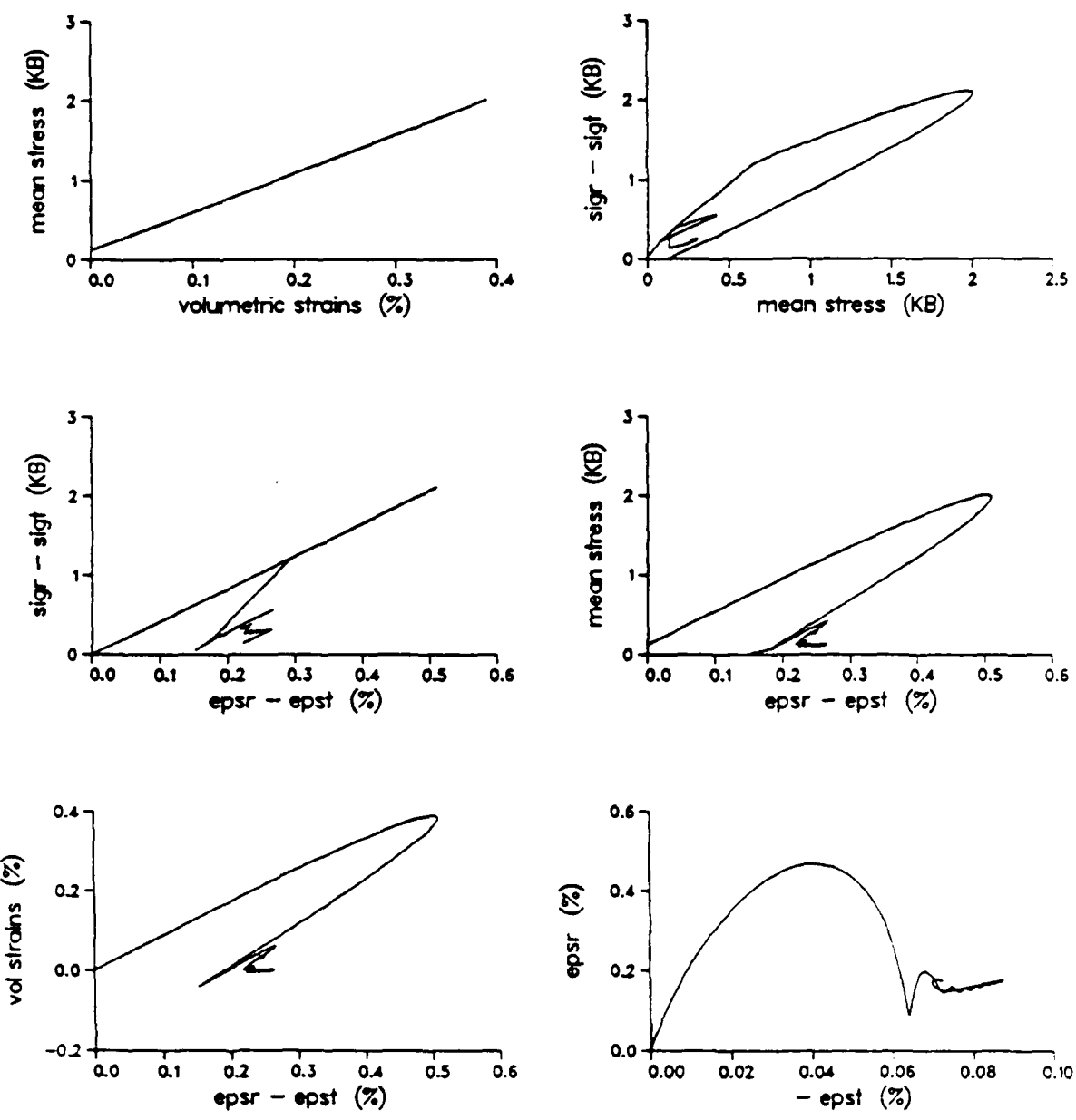


Figure B.9. Strain paths at 204 meters for high laboratory strength calculation – radial return flow rule.

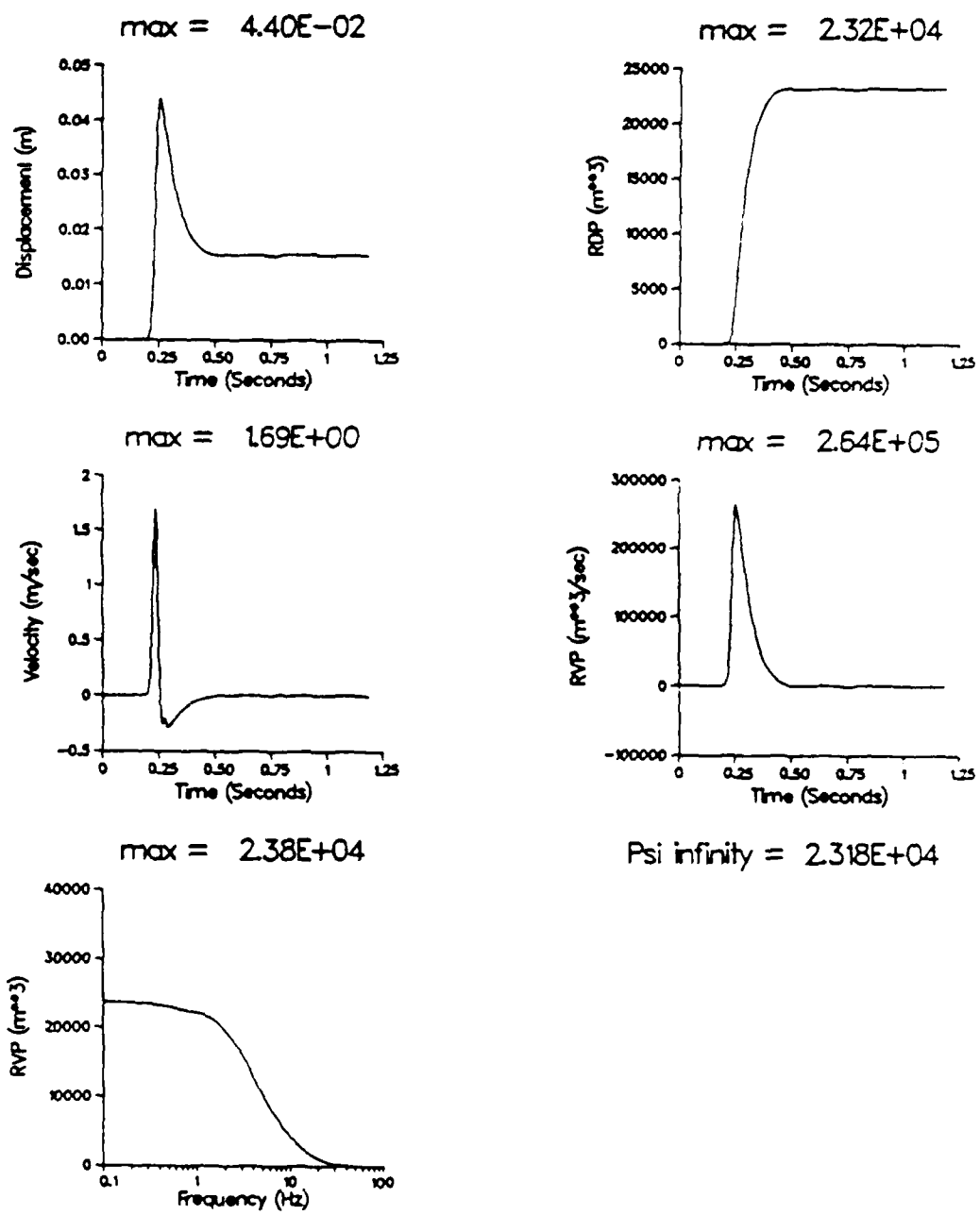


Figure B.10. Reduced displacement potential, reduced velocity potential, and displacement and velocity at 1225 meters for high laboratory strength calculation - associated flow rule

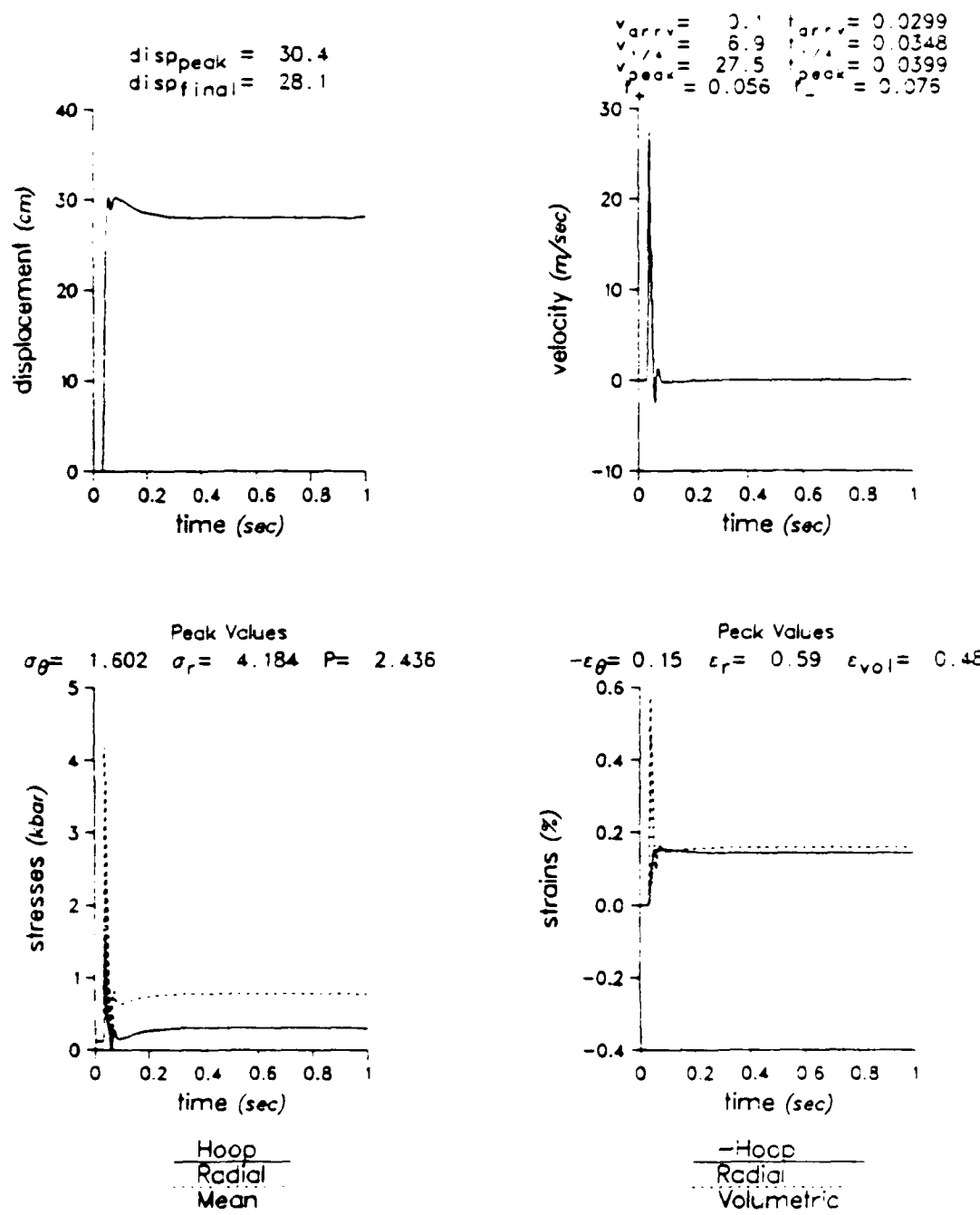


Figure B.11 Displacement, velocity, stress and strain time histories at 204 meters for high laboratory strength calculation - associated flow rule.

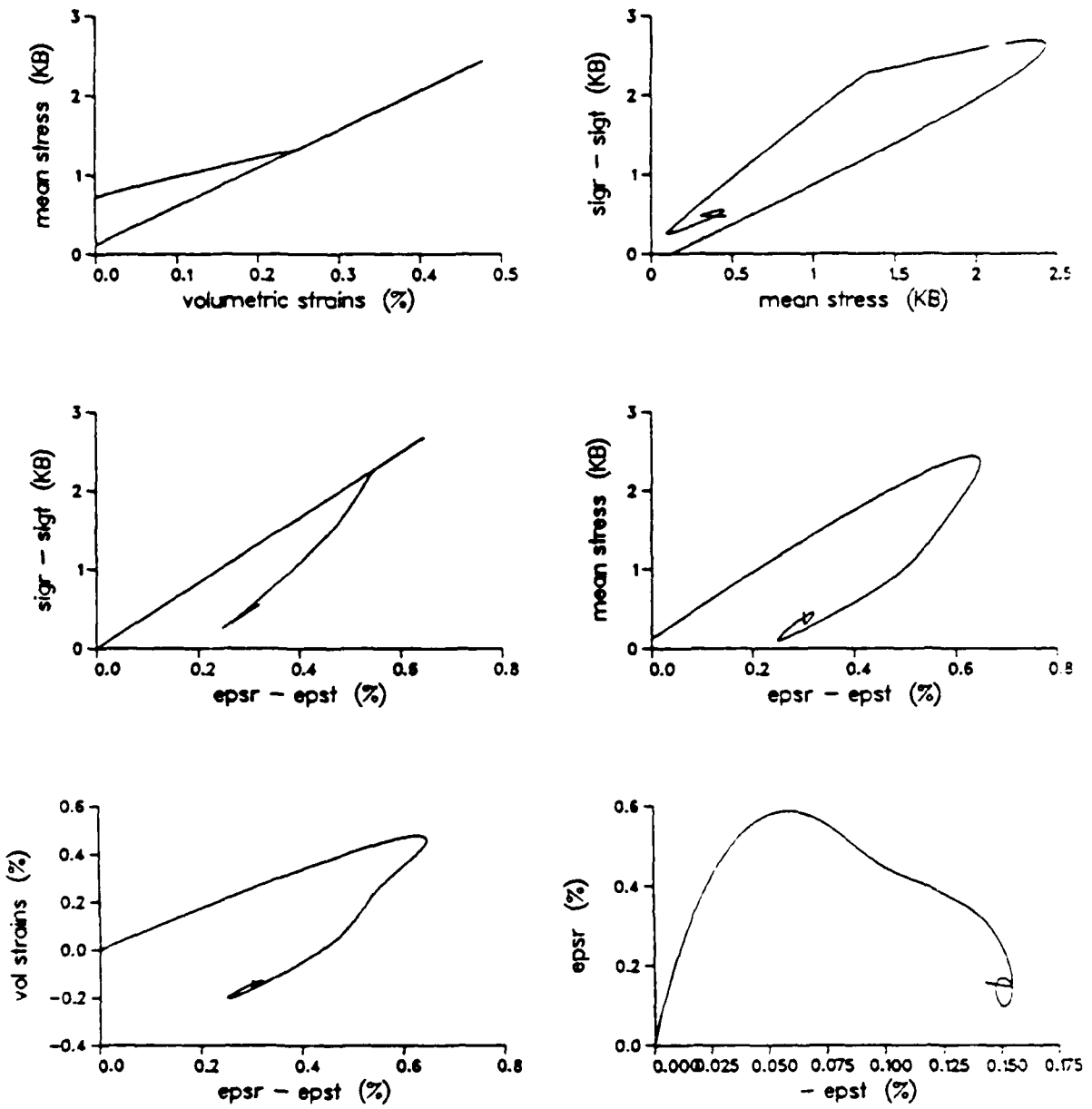


Figure B.12. Strain paths at 204 meters for high laboratory strength calculation - associated flow rule.

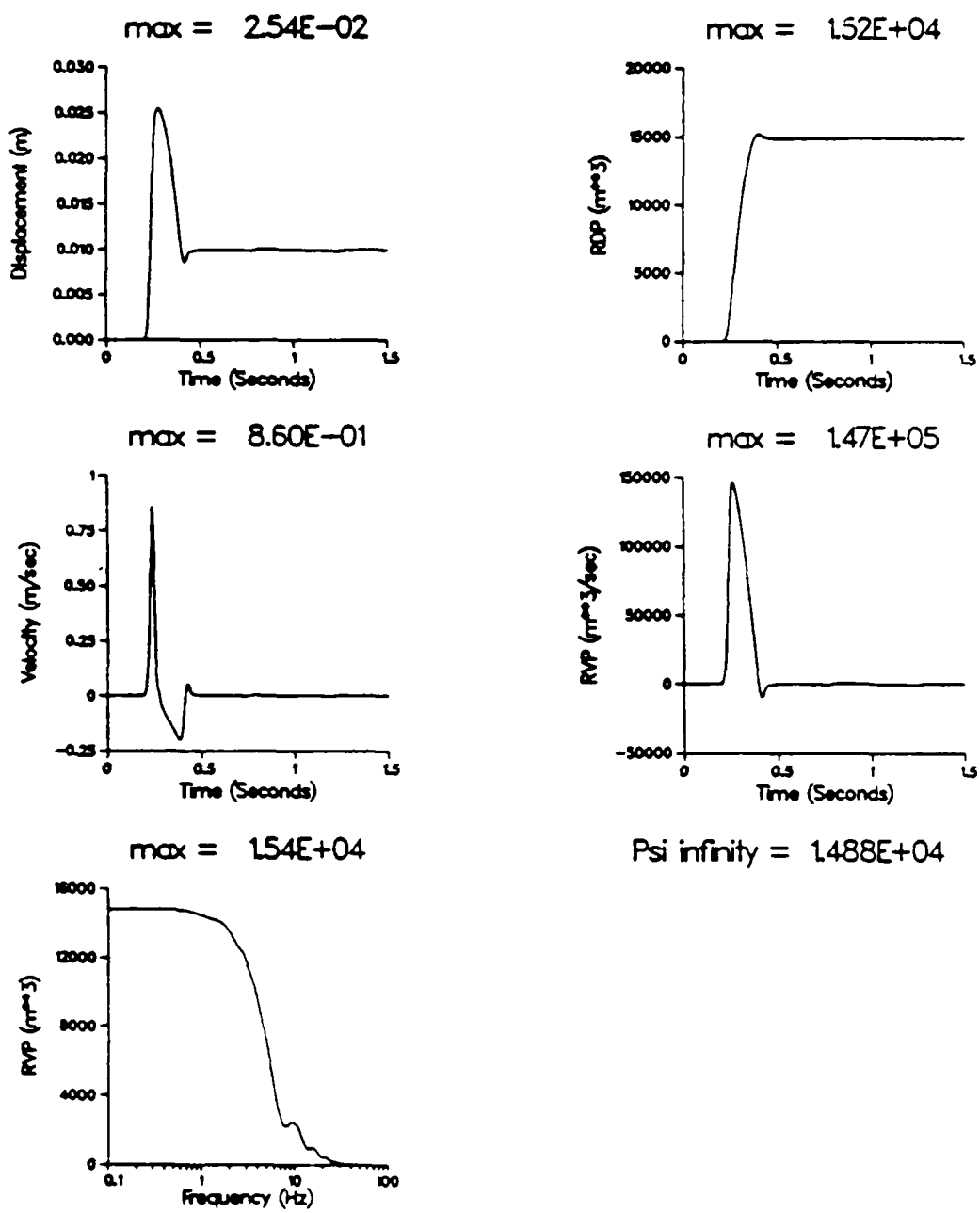


Figure B.13. Reduced displacement potential, reduced velocity potential, and displacement and velocity at 1225 meters for calculation with a linear failure surface with a slope of 0.5 - radial return flow rule

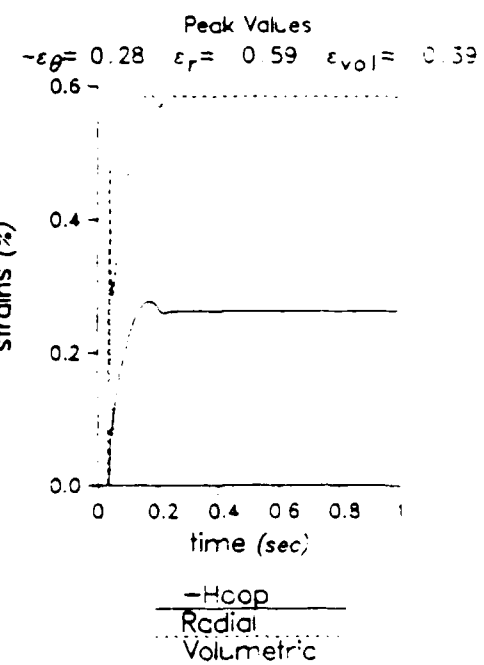
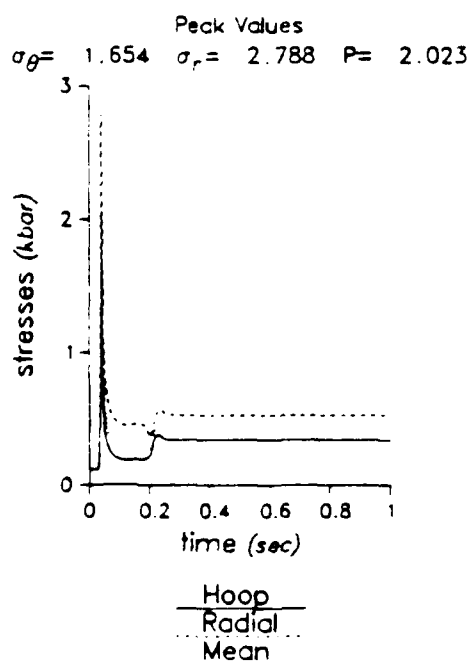
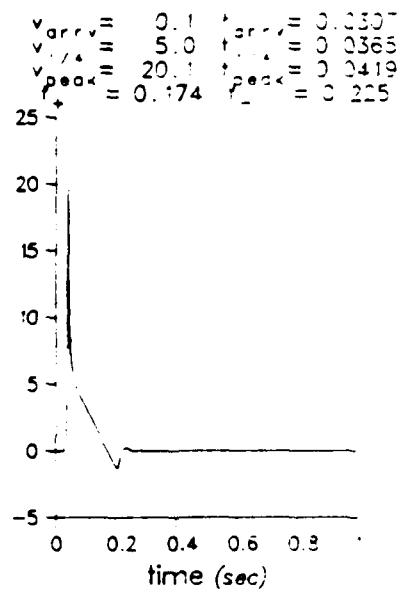
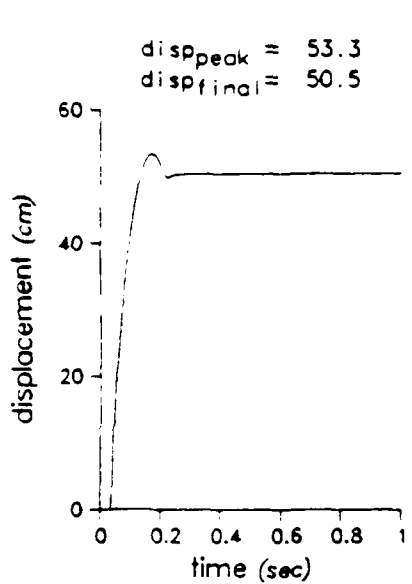


Figure B.14. Displacement, velocity, stress and strain time histories at 204 meters for calculation with a linear failure surface with a slope of 0.5 - radial return flow rule.

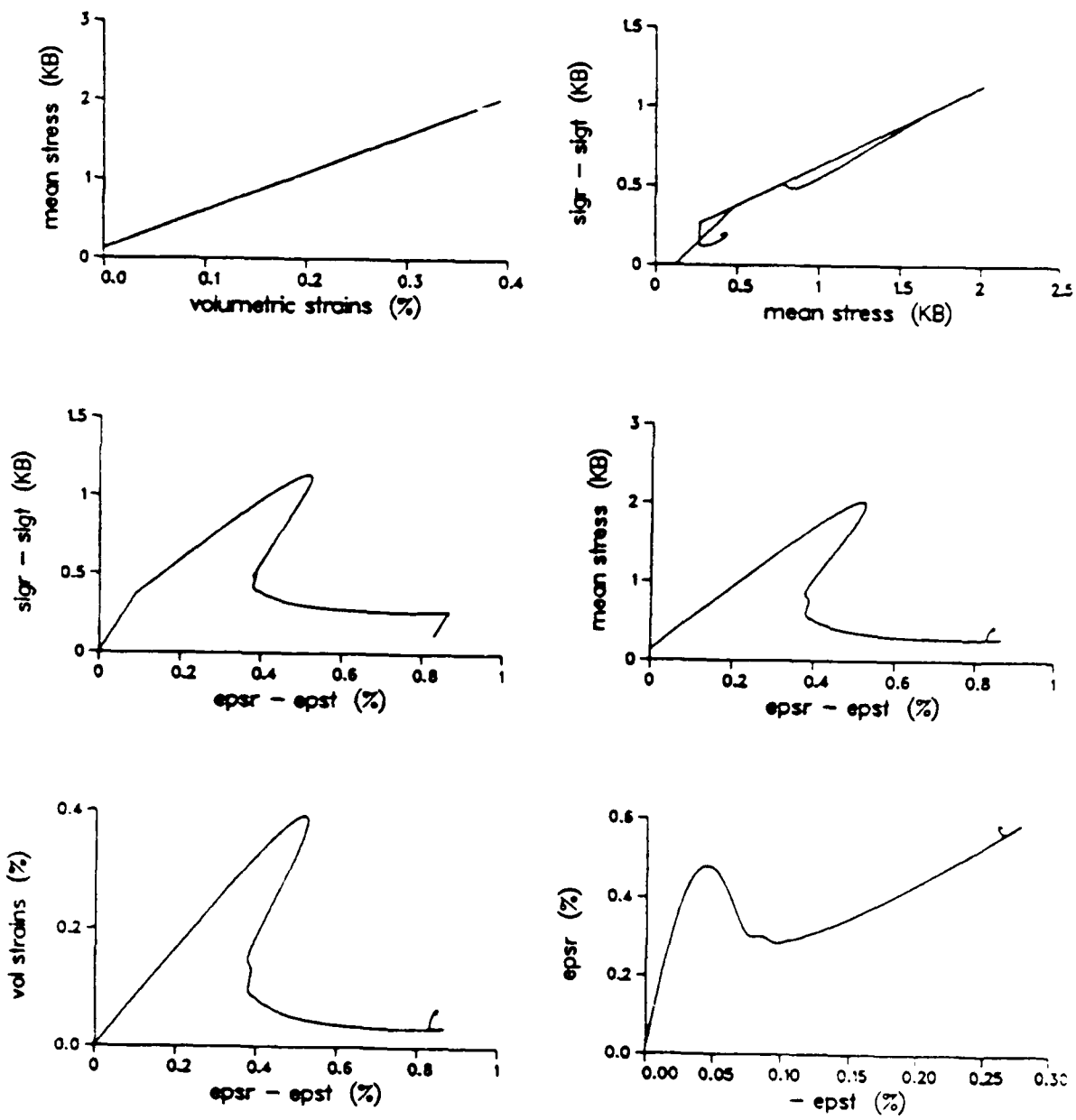


Figure B 15. Strain paths at 204 meters for calculation with a linear failure surface with a slope of 0.5 - radial return flow rule.

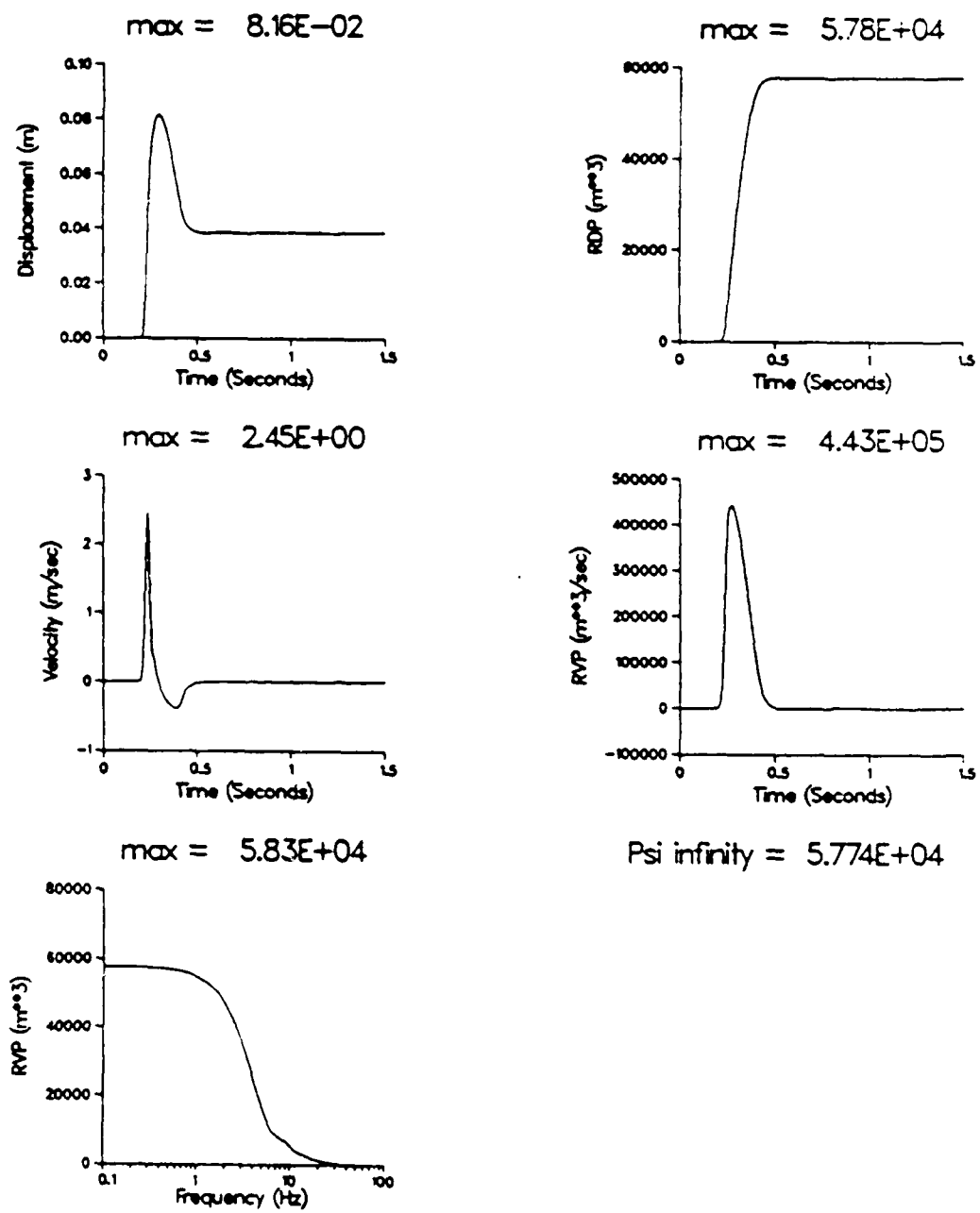


Figure B.16 Reduced displacement potential, reduced velocity potential and displacement and velocity at 1225 meters for calculation with a linear failure surface with a slope of 0.5 – associated flow rule.

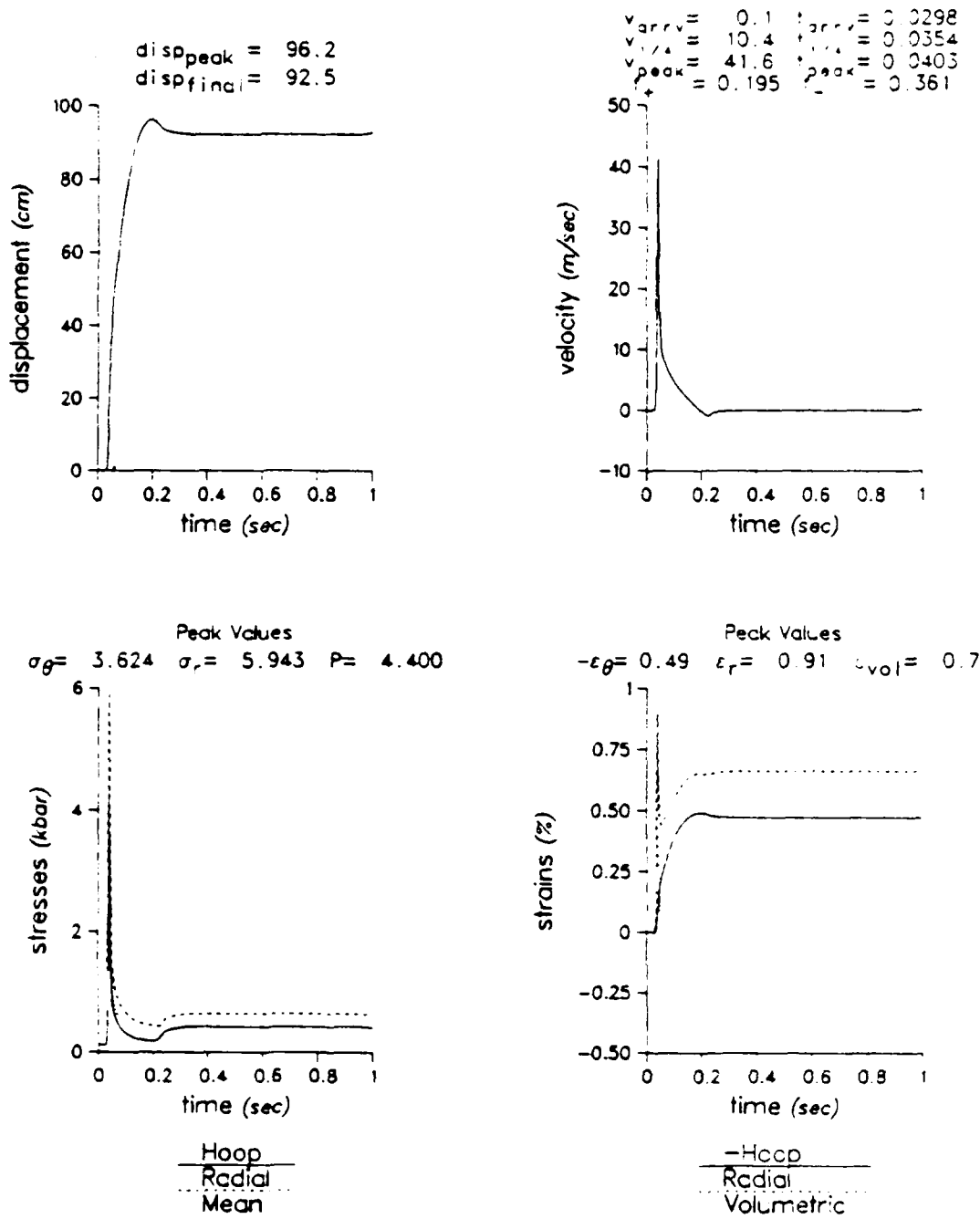


Figure B.17 Displacement, velocity, stress and strain time histories at 204 meters for calculation with a linear failure surface with a slope of 0.5 - associated flow rule.

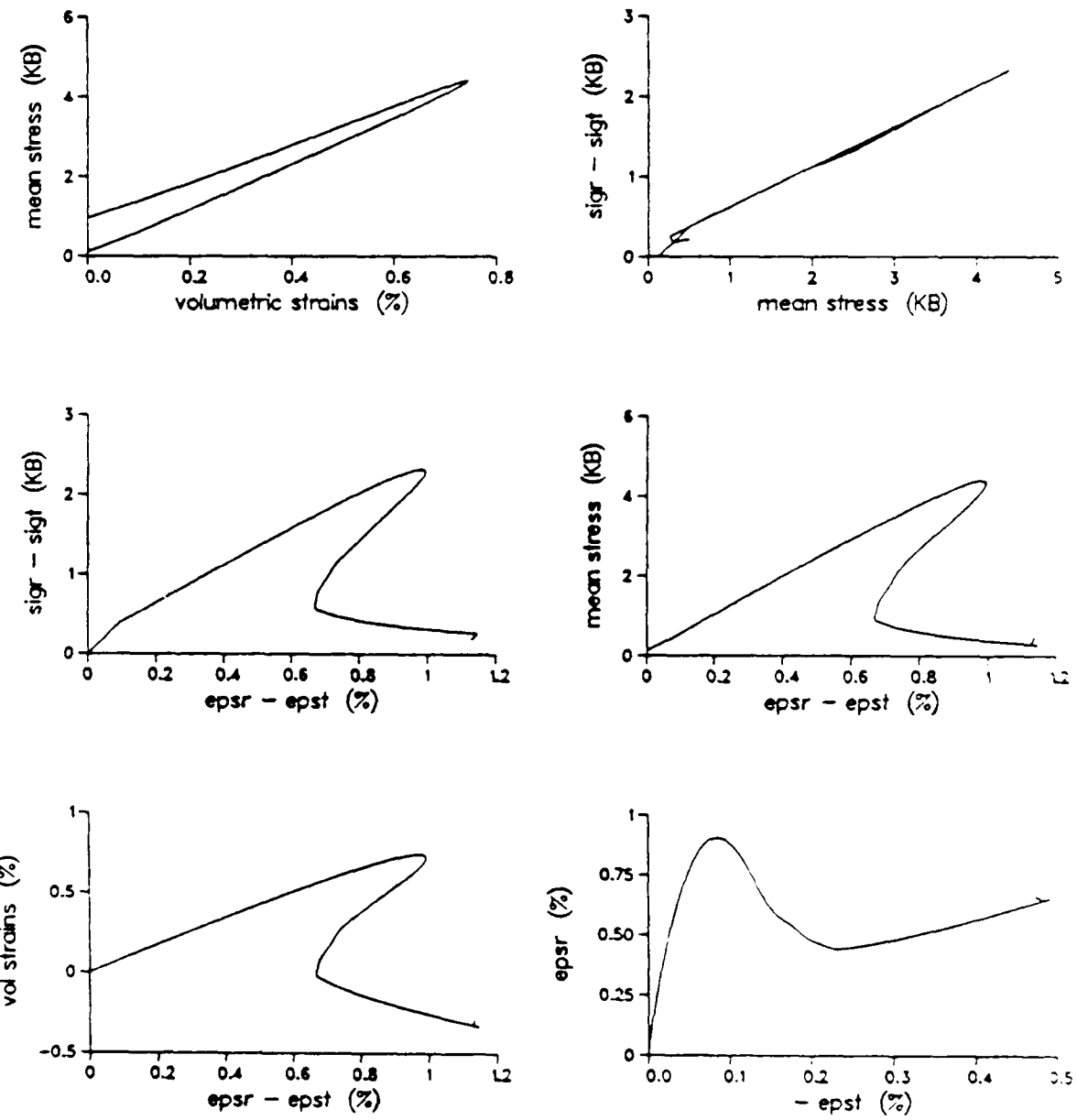


Figure B.18. Strain paths at 204 meters for calculation with a linear failure surface with a slope of 0.5 – associated flow rule.

END

4 - 07

DTIC